School of Chemistry

Fabrication and Evaluation of a Polycrystalline Diamond Schottky Diode for Low-Energy Beta Detection

Julia Collier

This thesis is submitted in partial fulfilment of the requirements for the Honours Degree of MSci Chemistry with Year Abroad at the University of Bristol

APRIL 2026

Supervisor: Prof. Neil Fox
Second Assessor: Prof. Paul May
Physical and Theoretical Chemistry
Word Count: $\sim$ 15,000

Abstract

Accurate detection of low-energy beta emitters, such as tritium, nickel-63, carbon-14, and promethium-147, is critical for environmental monitoring, nuclear safety, and fusion systems. Whilst existing semiconductor devices offer compactness and real-time operation, their sensitivity to low energy beta radiation is limited by spectral noise. Polycrystalline diamond offers significant advantages in spectral noise reduction, however the effects of grain boundaries and defect states on device performance remain poorly understood.

This work fabricated and evaluated a polycrystalline diamond Schottky diode as a low-energy beta detector with a M–I–p^+–M configuration. CASINO simulations highlighted that average penetration depth increases with incident beta energy, with 130 nm depth for tritium and 19.2 µm for promethium-147. Aluminium exhibited a low backscattering coefficient of 0.14, indicating suitability as a Schottky contact, however a layer below 35 nm is required for 90% of tritium beta particle energy to be deposited within the active region of the device. The fabrication process employed a 532 nm laser to etch a thin membrane of 33µm in intrinisc diamond layer with minimal surface damage indicated by SEM. Raman spectra revealed a prominent diamond peak at 1332 cm^{-1} with FWHM of 7.9 cm^{-1} characteristic of polycrystalline diamond, however no boron features were present for boron doped p^+ diamond.

Beta particle irradiation was conducted using a Kimball Physics EGF-3104 electron gun. Initial testing at 5.7 keV incident energy demonstrated a threshold voltage of 0 V, a maximum forward current of 1.04 µA and a rectification ratio of 3.2. A clear hysteresis was observed, indicative of localised carrier trapping at grain boundaries. Surface damage to the Schottky contact precluded further device operation, however following acid-based contact removal and re-deposition, rectification was recovered with a smaller maximum current of 0.58 µA, same turn on voltage at 0 V and rectification ratio of 3.2. No hysteresis was observed, attributed to improved junction uniformity following acid cleaning during contact removal.

Current–voltage measurements across 1–20 keV incident electron energy showed energy-dependent response, with stable operation from 7–20 keV and instability at 1–6 keV, giving a discrimination limit of 6 keV. No hysteresis was observed across energies, indicating an intact Schottky barrier. This work demonstrates the potential of polycrystalline diamond Schottky diodes for low-energy beta detection, however further optimisation is required to improve performance.

Acknowledgements

Prof. Neil Fox; from my personal tutor in my first year, to my lab supervisor in my last; I have enjoyed working with you throughout my degree. Thank you for giving me the opportunity to see what I am capable of.

Dr Ramiz Zulkharnay; thank you for training me on much of the lab equipment, in particular the back reactor, SEM, and Pt/Pd sputter coater. I am grateful for the help, the advice, and for you and Gulnur making the early mornings in the lab even more enjoyable.

Thankyou to Catherine Monk, who trained me on the laser for the membranes, Dr. Liam Cullingford who helped with the e-beam, to Dr. James Smith, who always lends a hand when everything goes wrong. Thank you also to the fellow budgies in the diamond group for the sense of community, and in particular to Sarah, Elâ, as well as Simran; for enduring the many hours of laser operation together and Thomas; for sharing the burden of band diagrams and anything remotely physics related.

To my family; Babciu; nareszcie udało mi sie zdobyć dyplom, Brian; thankyou for the support you have consistently provided. To Splashes for the start of my journey, and Rubix for the end. And finally, to my mum; there are not enough diamonds in the world to do justice to all the help you have given me.

Author’s Declaration

I declare that the work in this dissertation was carried out in accordance with the requirements of the University’s *Regulations and Code of Practice for Research Degree Programmes* and that it has not been submitted for any other academic award. Except where indicated by specific reference in the text, the work is the candidate’s own work. Work done in collaboration with, or with the assistance of, others, is indicated as such. Any views expressed in the dissertation are those of the author.

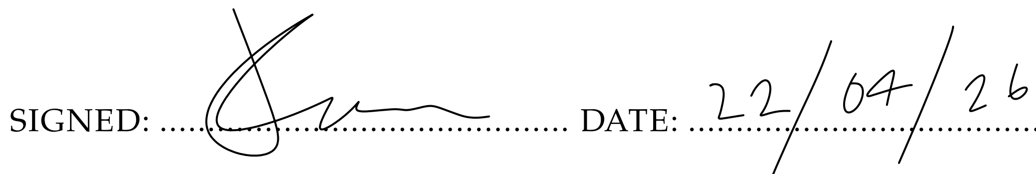

Contents

Chapter 1: Introduction ... 11
1.1 Global Relevance ... 11
1.1.1 *Radioisotope Detection* ... 11
1.1.2 *Betavoltaic Batteries* ... 11
1.2 Beta Spectroscopy ... 11
1.2.1 *Beta Energy Spectra* ... 12
1.3 Current Technology ... 13
1.3.1 *Efficiency* ... 14
1.3.2 *Energy Resolution* ... 14
1.3.3 *Spectral Noise* ... 14
1.3.4 *Real Time monitoring* ... 15
1.3.5 *Practicality* ... 15
1.3.6 *Motivation for a Novel Semiconductor Detector* ... 15
1.4 Schottky Diodes ... 16
1.4.1 *Operational Principles* ... 16
1.4.2 *Biasing* ... 17
1.4.3 *Current–Voltage Characteristics* ... 18
1.5 Diamond ... 19
1.5.1 *Properties* ... 19
1.5.2 *Limitations of Diamond as a Semiconductor* ... 20
1.6 Thesis Aims & Device Concept ... 21

Chapter 2: CASINO Simulations ... 22
2.1 Introduction ... 22
2.2 Simulation Parameters ... 22
2.3 Results & Discussion ... 23
2.3.1 *Beta penetration depth* ... 23
2.3.2 *Backscattering* ... 24
2.3.3 *Schottky metal thickness* ... 25
2.4 Concluding Remarks ... 26

Chapter 3: Fabrication ... 27
3.1 Substrate Preparation ... 27
3.1.1 *Acid pre-treatment* ... 27
3.1.2 *Laser cutting* ... 27

3.2 Diamond Membrane 28
3.2.1 Laser etching 28
3.2.1.1 Sonication 29
3.2.2 H-plasma CVD 29
3.3 Ohmic Contact 31
3.3.1 Boron Doped Diamond CVD 31
3.3.2 H-termination 33
3.3.3 Pt/Pd Metal Deposition 34
3.4 Schottky Contact 35
3.4.1 O-termination 35
3.4.2 Al Deposition 36

Chapter 4: Characterisation 37
4.1 LEXT 37
4.1.1 Overview 37
4.1.2 Data Acquisition 37
4.1.3 Results & Discussion 37
4.1.3.1 LEXT Images 37
4.1.3.2 Cross-Section Depth Profile 38
4.2 Raman 39
4.2.1 Overview 39
4.2.2 Data Acquisition 40
4.2.3 Results & Discussion 40
4.2.3.1 BDD 40
4.2.3.2 Laser Treatment 41
4.3 SEM 42
4.3.1 Overview 42
4.3.2 Data Acquisition 43
4.3.3 Results & Discussion 43
4.3.3.1 After Laser Treatment and H-Plasma CVD 43
4.3.3.2 After BDD Growth 44

Chapter 5: Device Performance 46
5.1 Electron Gun 46
5.1.1 Overview 46
5.1.2 Data Acquisition 46
5.2 Initial Performance 48
5.2.1 5.7 keV 48
5.2.1.1 Rectification Ratio 48
5.2.1.2 Hysteresis 49

5.3 Device Failure 49
5.4 Device Recovery 50
5.4.1 5.7 keV 50
5.4.1.1 Hysteresis 51
5.4.1.2 Rectification Ratio 51
5.4.2 1–20 keV 52
5.4.2.1 Rectification Ratio 53
Chapter 6: Conclusions & Future Work 55
6.1 Conclusions 55
6.2 Future work 56
Chapter 7: Appendix 64

List of Tables

1.1 Table displaying typical characteristics of four radioisotopes: Tritium-3, Nickel-63, Carbon-14 and Promethium-147. 13
1.2 Key properties of common semiconductor materials [1]. 20

2.1 Densities of the materials used in CASINO simulations. 22
2.2 Parameters used in the CASINO simulation software. 22
2.3 Representative energies of low-energy beta-emitting radioisotopes used for CASINO simulations. 23
2.4 Maximum and average penetration depths of simulated electrons in diamond at different incident energies. 23

3.1 Laser machining parameters used for membrane fabrication. 29
3.2 Hydrogen plasma CVD parameters for graphite etching. 31
3.3 CVD parameters for boron doped diamond growth. 33
3.4 Hydrogen plasma CVD parameters for H-termination. 34

4.1 Centre position and full width at half maximum (FWHM) of the diamond Raman peak before and after BDD growth. The small increase in FWHM after BDD growth suggests a marginal increase in disorder, defect density, or lattice strain. 41
4.2 Peak positions and full width at half maximum (FWHM) values obtained from the Raman spectrum of the laser-treated membrane surface prior to BDD growth. The broad linewidths indicate a high degree of structural disorder and a distribution of non-diamond carbon phases across the surface. 42

5.1 Operating parameters of Electron Gun operation 47
5.2 Rectification behaviour of the device at ±20 V 49
5.3 Rectification behaviour at ±20 V of diode before and after re-deposition 52

7.1 Rectification ratio at ±20 V for energies 1–20 keV 64

List of Figures

1.1 Schematic illustrations of two forms of beta particle emission. β^+ decay is depicted in (a) where a proton (red) converts to a neutron (pink) with the emission of a positron (orange) and neutrino (purple). β^- decay is depicted in (b) where a neutron converts to a proton with the emission of an electron (yellow) and antineutrino (blue). 12

1.2 The β particle energy spectra of four radioisotopes: (a) Tritium-3, (b) Nickel-63, (c) Carbon-14 and (d) Promethium-147. Adapted from Ref [2]. 13

1.3 Band structure of a metal/p-type semiconductor Schottky junction (a) before contact and (b) after contact at thermal equilibrium. Before contact, the metal and semiconductor are electrically isolated and have independent Fermi levels and work functions. After contact, charge redistribution leads to Fermi-level alignment, band bending, and formation of the Schottky barrier at thermal equilibrium. E_{vac} denotes the vacuum level, E_C and E_V are the conduction and valence band edges, and E_F is the Fermi level (where E_{FM} and E_{FS} correspond to the metal and semiconductor, respectively). Φ_M and Φ_S are the metal and semiconductor work functions, Φ_b is the Schottky barrier height, and V_b is the built-in potential. 16

1.4 Schematic of charge generation and collection in a Schottky diode under beta particle irradiation. Incident β particles generate electron–hole pairs within the depletion region of the semiconductor. The built-in electric field (E) separates the carriers, with electrons drifting towards the Schottky contact and holes towards the ohmic contact. 17

1.5 Energy band diagrams of a metal/p-type semiconductor Schottky junction under applied bias. (a) Forward bias reduces the effective barrier height by $V_b - V_f$, narrowing the depletion region and facilitating majority carrier transport across the interface. (b) Reverse bias increases the barrier to $V_b + V_r$, widening the depletion region and suppressing carrier flow. E_C and E_V denote the conduction and valence band edges, E_{FM} is the metal Fermi level, Φ_b is the Schottky barrier height, and V_b is the built-in potential. 18

1.6 Idealised current–voltage (I–V) characteristics of a Schottky diode, illustrating rectifying behaviour. Under forward bias, the current increases exponentially once the applied voltage exceeds the threshold voltage, V_{Th}, due to reduction of the Schottky barrier and enhanced carrier transport. Under reverse bias, a small leakage current is present prior to breakdown, arising from thermionic emission and generation of electron–hole pairs (EHPs) within the depletion region. At sufficiently high reverse bias, the current increases sharply at the breakdown voltage, V_{BD}, due to avalanche breakdown. 19

1.7 Schematic of the polycrystalline diamond Schottky diode structure fabricated in this work. From top to bottom, the device comprises a Schottky metal contact (orange), an intrinsic polycrystalline diamond layer containing a locally thinned membrane region (grey), a boron-doped diamond layer (blue), and an ohmic back contact (purple). The membrane is incorporated to enhance sensitivity to low-energy beta particles by reducing the charge carrier drift distance to the electrodes. 21

2.1 Simulated electron trajectories in diamond for increasing incident energies: (a) 5 keV, (b) 20 keV, (c) 50 keV, and (d) 60 keV. Higher energy electrons exhibit increased penetration depth and lateral spread, with more extensive scattering pathways. Incident trajectories are shown in red, while scattered electron paths within the diamond are shown in blue. 24
2.2 Backscattering coefficients of 5 keV beta particles for different metals. Higher atomic number metals (Au, Pt) exhibit significantly greater backscattering compared to lower atomic number materials such as Al, indicating reduced electron transmission into the diamond for high-Z contacts. 25
2.3 Energy deposition depth in diamond across varying aluminium thickness: (a) 10 nm; (b) 22.5 nm; (c) 35 nm; (d) 40 nm. The region where 90% energy is deposited is shown shaded region in red. The legend in (a) applies to all graphs. 26

3.1 Photograph of the Oxford Lasers Alpha 532 laser micromachining system used to cut and etch the diamond substrate using programmed scan templates. 27
3.2 Representation of the laser scan template used in Cimita software for membrane fabrication, showing a cross-hatched rastering pattern to maximise uniform material removal. 28
3.3 Photograph of the Microwave plasma chemical vapour (MW-CVD) Astek type reactor used for undoped diamond growth, with key components indicated. 30
3.4 Photograph of the substrate inside the undoped MW-CVD reactor during (a) start and (b) end of H-plasma treatment. 31
3.5 Photograph of the Microwave plasma chemical vapour (MW-CVD) Astek type reactor used for boron-doped diamond growth, with key components indicated. 32
3.6 Photograph of masked boron doped diamond MW-CVD growth 32
3.7 Shadow masks used for metallisation: (a) Pt/Pd deposition mask and (b) Al deposition mask. 34
3.8 Photograph of the AGAR Scientific sputter coater used for Pt/Pd deposition, with key controls indicated. 35
3.9 Photograph of the Jelight 42 UVO-cleaner equipment used for oxygen termination, with key components indicated. 36
3.10 Photograph of the Baltzer system in physics used by Prof. Neil Fox to deposit 22.5 nm of aluminium onto the sample for the formation of the Schottky contact. 36

4.1 Completed polycrystalline diamond device. (a) Optical image showing the membrane region, intrinsic diamond, boron-doped diamond, Pt/Pd ohmic contact, and the 22.5 nm Al Schottky contact on the reverse side. (b) Three-dimensional depth image of the membrane region, with the colour scale indicating surface height. 38
4.2 The cross section depth profile of the diamond membrane, indicating a final thickness of 33 µm. 39
4.3 Raman spectra of the membrane surface (a) before and (b) after boron-doped diamond (BDD) growth. In both cases, a sharp peak at 1332 cm^{-1} is observed, corresponding to the first-order diamond Raman mode. . . 40
4.4 Raman spectrum of the laser-treated membrane surface prior to BDD growth. Bands at 1354 and 1554 cm^{-1} correspond to the D and G bands respectively, indicating the formation of sp^2-bonded carbon. Broad features at 782 and 980 cm^{-1} are associated with amorphous or nano-carbon phases. 42
4.5 SEM micrographs of the laser-etched diamond membrane following H-plasma treatment. (a) Whole membrane, illustrating the stepped profile arising from sequential laser passes. (b) Wall region showing periodic microgrooves associated with the laser scan path. (c) Central membrane region, displaying a comparatively smooth surface indicative of effective post-processing. (d) Periphery of the membrane, where increased roughness and residual microgrooves from laser etching persist. 44
4.6 SEM micrographs of the laser-etched diamond membrane following boron-doped diamond (BDD) growth. (a) Membrane wall, where periodic microgrooves and stepped laser profile remained evident. (b) Peripheral membrane surface, where roughness and laser-induced microgrooves were retained. 45

5.1 Electron-beam irradiation setup used for device testing, with key components indicated. 47
5.2 Current–voltage characteristics under dark conditions and under 5.7 keV electron irradiation. An increase in current is observed under irradiation in both forward and reverse bias, indicating successful generation and collection of charge carriers within the device. 48
5.3 Dark current–voltage (I–V) characteristics of the device following degradation. The absence of rectification and the presence of low, unstable currents indicate failure of the Schottky junction. 50
5.4 Current–voltage characteristics of the device before and after re-metallisation of the aluminium Schottky contact, under dark conditions and 5.7 keV irradiation. The restored rectifying behaviour confirms recovery of the Schottky junction following contact re-deposition. 51
5.5 Current–voltage characteristics under dark conditions and under electron irradiation of energies 1–20 keV. An increase in current is observed under irradiation in both forward and reverse bias, indicating successful generation and collection of charge carriers within the device. 53
5.6 Rectification ratio measured at $\pm$20 V from current–voltage characteristics recorded under incident electron beam energies of 1–20 keV. . . . 54

Chapter 1: Introduction

1.1 Global Relevance

1.1.1 Radioisotope Detection

Nuclear energy is widely considered a low-carbon energy source [3], with nuclear fusion attracting particular interest as a future technology [4]. Fusion systems rely on radioactive tritium as a fuel, while nuclear fission generates radioactive waste streams that must also be monitored and controlled. In both cases, the detection and discrimination of radioactive isotopes is important for worker safety, waste management, regulatory compliance [4–9], and protection against theft or illicit trafficking of radioactive material [10]. This can be achieved *via* beta detection, where radionuclides are distinguished through their characteristic beta emission spectra. However, tritium emits very low-energy beta particles and is therefore notoriously difficult to detect. This has motivated the development of detectors with sufficient sensitivity to resolve tritium, in addition to other low-energy beta-emitting radioisotopes as this enables discrimination between isotopes.

1.1.2 Betavoltaic Batteries

Betavoltaic cells are small, portable batteries that couple a radioactive beta-emitting source to a semiconductor junction, converting emitted beta particles into usable electrical current. Their long lifetimes depend on the half-life of the radioisotope used as the beta source [11, 12], making them attractive for applications where battery recharging is difficult, such as medical implants [13], sensors [13], aviation [14], underwater environments [15], and spacecraft satellites [16–18]. The radioactive power source is typically a low-energy beta emitter, as this reduces radiation damage to the semiconductor material. Commonly investigated sources include tritium (^{3}H) [19–23], nickel-63 (^{63}Ni) [20, 21, 24–29], promethium-147 (^{147}Pm) [12], and carbon-14 (^{14}C) [12]. Although betavoltaic devices are intended for power generation rather than beta spectroscopy, both rely on efficient charge generation and collection from low-energy beta particles in a semiconductor junction.

1.2 Beta Spectroscopy

Beta radiation consists of high-speed charged particles emitted during radioactive decay. Beta particles are emitted via two pathways: beta-plus (β^{+}) decay and beta-minus (β^{-}) decay, as illustrated in Figure 1.1. In the former, a proton is converted into a neutron, emitting a positron (β^{+} particle) and an electron neutrino. The positron may undergo further decay by annihilating with an electron to produce two 511 keV gamma photons [30]. In beta-minus decay, a neutron is converted into a proton, emitting an electron (β^{-} particle) and an electron antineutrino.

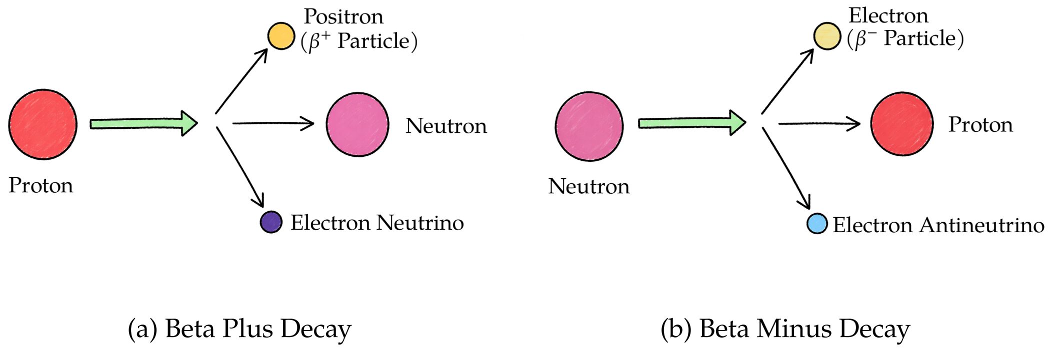

(a) Beta Plus Decay

(b) Beta Minus Decay

Figure 1.1: Schematic illustrations of two forms of beta particle emission. β^+ decay is depicted in (a) where a proton (red) converts to a neutron (pink) with the emission of a positron (orange) and neutrino (purple). β^- decay is depicted in (b) where a neutron converts to a proton with the emission of an electron (yellow) and antineutrino (blue).

The kinetic energy of nuclear decay is shared between the beta particle and the (anti)neutrino in varying proportions: the beta particle may adopt an energy value between zero and the maximum decay energy, E_{max}, with the remaining energy carried by the neutrino [31]. This results in a continuous distribution of electron energies ranging from zero up to a characteristic endpoint energy, as opposed to the discrete energies typically observed in alpha or gamma spectroscopy [32]. Although this continuous distribution complicates isotope identification, the characteristic endpoint and average energies of a given radionuclide still allow identification through analysis of its beta spectrum [2]. While beta spectroscopy can be applied to both positrons and electrons [30], this work focuses on β^- decay, as it is the relevant pathway for the low-energy radionuclides used in radioisotope detection and betavoltaic applications.

1.2.1 *Beta Energy Spectra*

The beta energy spectra of the representative isotopes considered in this work—tritium (^{3}H), nickel-63 (^{63}Ni), carbon-14 (^{14}C), and promethium-147 (^{147}Pm)—are shown in Figure 1.2, with data obtained from the International Atomic Energy Agency (IAEA) database [33]. They display discrete average and end point energies (E_{max}), which are summarised in Table 1.1. In particular, the low beta energies of tritium make it especially challenging to detect. Furthermore, the significant overlap between the low-energy regions of the beta spectra highlights the need for a detector with sufficient energy resolution to distinguish between radioisotopes.

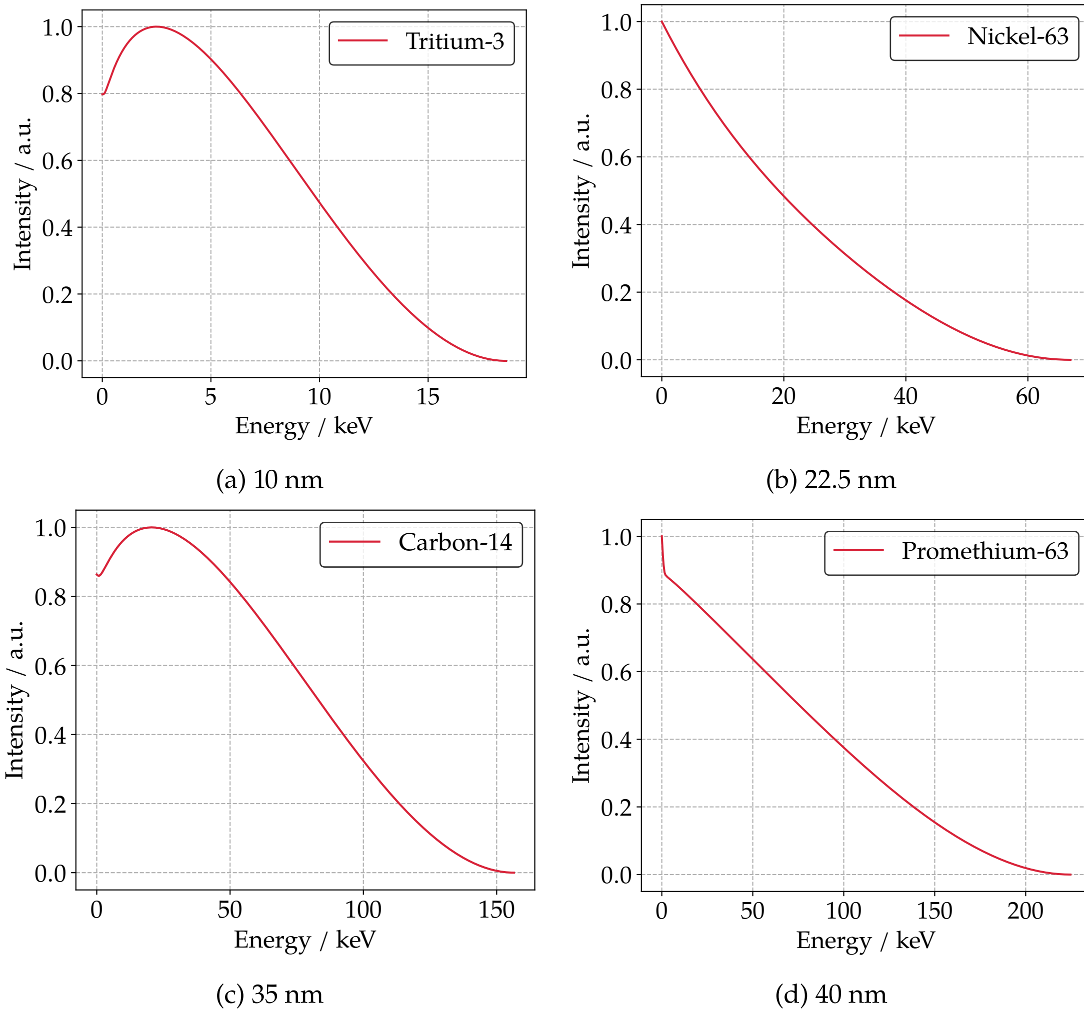

Figure 1.2: The β particle energy spectra of four radioisotopes: (a) Tritium-3, (b) Nickel-63, (c) Carbon-14 and (d) Promethium-147. Adapted from Ref [2].

Table 1.1: Table displaying typical characteristics of four radioisotopes: Tritium-3, Nickel-63, Carbon-14 and Promethium-147.

	H-3	**Ni-63**	**C-14**	**Pm-147**
Average energy / keV	5.68	17.43	49.47	61.93
End point energy / keV	18.59	66.95	156.48	224.50

1.3 Current Technology

Low-energy beta spectroscopy is primarily carried out using three main detector classes: liquid scintillation counters (LSCs), gas-filled detectors, and semiconductor detectors. Liquid scintillation counters (LSCs) detect beta particles through light emitted by an excited scintillation medium [34], gas-filled detectors rely on ionisation produced in a gas volume [35, 36], and semiconductor detectors operate by collecting electron–hole pairs (EHPs) generated within a

solid-state material [37]. Each offers a different balance of detection efficiency, energy resolution, noise performance, real-time capability, and practical deployment, which are assessed in the following section.

1.3.1 Efficiency

Defined as the fraction of emitted radiation that is successfully detected, LSCs have exhibited high efficiencies of 63% [38] and 70% [39] for unquenched, low-energy tritium samples. However, this decreases to 35% under quenched conditions, where impurities in the sample mixture reduce the scintillation response [39]. Further, values as low as 5% have been reported for severely quenched samples [40], highlighting a strong dependence on sample composition. Specialised gas-filled detectors can achieve moderate efficiencies of 55%–60% for tritium in air [41]. In contrast, semiconductor devices demonstrate the lowest efficiencies of up to 45% for tritium at near-zero source–detector separation, but decrease to 30% at a distance of 0.5 mm [42], indicating a strong dependence on device positioning. Although LSCs can provide the highest efficiencies under ideal conditions, a major drawback is their strong dependence on sample preparation, whereas semiconductor devices avoid this limitation by providing a solid state architecture. Thus, a clear advantage of semiconductor detectors is the that they require minimal sample handling, despite their lower efficiency.

1.3.2 Energy Resolution

Characterised as the ability to distinguish between particles of similar energies, energy resolution determines the extent to which spectral endpoints are clearly resolved, therefore enabling unambiguous nuclide identification. Semiconductor detectors have the highest energy resolution even in the low energy 0–20 keV region [43, 44] as the low energy required to generate EHPs produces a large number of charge carriers that generate signals. In contrast, more energy is required to create electron-ion pairs, and so gas-filled detectors generate fewer charge carriers and have poorer resolution. The intrinsic energy resolution of scintillation detectors is limited by the non-proportionality of light yield with respect to the energy of incident radiation [45]. This makes semiconductor detectors the strongest option where spectroscopic performance is required, as they provide the clearest route to resolving low-energy beta spectra and distinguishing radioisotopes.

1.3.3 Spectral Noise

Signals not arising from beta particles, or fluctuations in the signal itself contribute to spectrum noise and should be minimised for optimal spectrometer performance. The noise may originate at the detector itself or at the readout electronics, or the interconnection between them [46]. In terms of detector noise, semiconductor devices display noise when thermally energy generates electron–hole pairs without the presence of beta particles. This forms a leakage current, defined as the current present even in the absence of incident radiation [47]. Gas-filled detectors exhibit low intrinsic noise due to their high ionisation energies;

however, this also limits their sensitivity to low-energy beta particles. LSCs display relatively low background noise but are affected by statistical fluctuations in photon production, photomultiplier tube noise, and chemical quenching effects, all of which contribute to spectral broadening [45]. This highlights a key limitation of conventional semiconductor detectors: despite superior spectral resolution, their performance can be compromised by thermally generated leakage current. However, this may be improved by using a semiconductor with a wider bandgap than conventional materials, which would retain the advantages of solid-state detection whilst reducing noise.

1.3.4 Real Time monitoring

Of the discussed technologies, only semiconductor detectors offer continuous, real time monitoring. Gas-filled detectors can offer near inline monitoring with short integration times of 90 s reported [48]; however, they rely on gas flow into the chamber, meaning performance can degrade in stagnant environments, particularly for low-energy beta emitters with short range in air. LSCs require sample preparation and do not offer real time monitoring [49]. Semiconductor detectors therefore provide the clearest advantage for applications requiring immediate, continuous measurement, making them more suitable for autonomous or in situ monitoring than LSCs or gas-filled systems.

1.3.5 Practicality

Straightforward implementation of a device across multiple platforms is highly desirable across a wide range of industries. By design semiconductor devices are portable and compact, and can be used in a variety of location with relative ease. In contrast, liquid scintillation counters require complex sample preparation, for which proper sample preparation is crucial, as contamination or improper handling can skew the results significantly. In addition, after the measurements, the liquid scintillation cocktail is organic radioactive waste that cannot be reused [50]. Similarly, gaseous detectors may require detector gases that are difficult to handle. From a practical perspective, semiconductor detectors are the most versatile of the three technologies, as they combine compactness, ease of integration, and real-time operation.

1.3.6 Motivation for a Novel Semiconductor Detector

Despite the strengths of these established approaches, current methods do not simultaneously offer high spectral resolution, real-time operation, low noise, and straightforward solid-state integration. However, it is clear that semiconductor detector offer great potential, and would be improved by selecting an appropriate architecture optimised for radiation detection. Furthermore, the spectral noise present in current semiconductor detectors highlight the need for an improved semiconductor material, which may inhibit thermally generated carriers with a wider band gap. In this work, these requirements are addressed through the use of diamond as the semiconductor material and a Schottky diode as the

device architecture.

1.4 Schottky Diodes

A Schottky diode is a semiconductor device containing a metal–semiconductor junction that exhibits rectifying behaviour due to the formation of a potential barrier at the interface. Their simple structure and suitability for semiconductor radiation detection have made Schottky diodes a promising device architecture for low-energy beta detection **??**.

1.4.1 Operational Principles

When a metal is brought into direct contact with a semiconductor, charge redistribution occurs due to the difference in work function and Fermi level between the two materials [51]. Carriers transfer across the interface until thermal equilibrium is established and the Fermi levels align. As a result, a depletion region forms in the semiconductor near the interface, where mobile carriers are removed and a net space charge remains due to ionised dopants. The space-charge region induces band bending, and establishes a built-in electric field across the junction. This field creates a potential barrier at the metal–semiconductor interface, known as the Schottky barrier. The Schottky barrier impedes the motion of charge carriers more strongly in one bias direction than in the other, thus giving rise to rectifying behaviour. The band alignment before and after contact formation is shown in Figure 1.3.

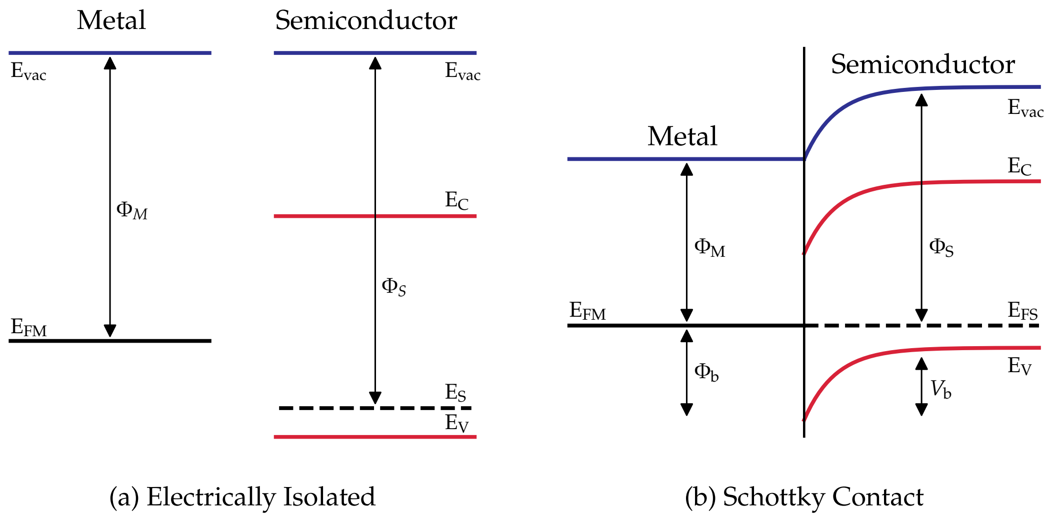

(a) Electrically Isolated

(b) Schottky Contact

Figure 1.3: Band structure of a metal/p-type semiconductor Schottky junction (a) before contact and (b) after contact at thermal equilibrium. Before contact, the metal and semiconductor are electrically isolated and have independent Fermi levels and work functions. After contact, charge redistribution leads to Fermi-level alignment, band bending, and formation of the Schottky barrier at thermal equilibrium. E_{vac} denotes the vacuum level, E_C and E_V are the conduction and valence band edges, and E_F is the Fermi level (where E_{FM} and E_{FS} correspond to the metal and semiconductor, respectively). Φ_M and Φ_S are the metal and semiconductor work functions, Φ_b is the Schottky barrier height, and V_b is the built-in potential.

In beta spectroscopy, incident beta particles deposit energy within the semiconductor, generating EHPs through ionisation. If these EHPs are created within the depletion region, the built-in electric field rapidly separates them: electrons drift towards the Schottky contact, while holes drift towards the ohmic contact. This charge separation induces a measurable current in the external circuit. This process drives the operation of the Schottky diode as a radiation detector and is illustrated in Figure 1.4.

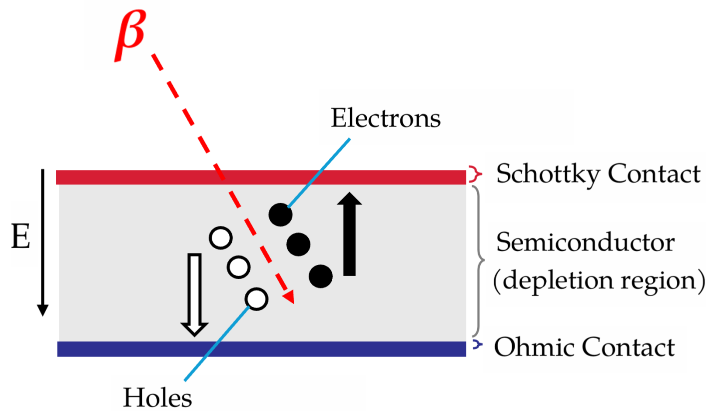

Figure 1.4: Schematic of charge generation and collection in a Schottky diode under beta particle irradiation. Incident β particles generate electron–hole pairs within the depletion region of the semiconductor. The built-in electric field (E) separates the carriers, with electrons drifting towards the Schottky contact and holes towards the ohmic contact.

1.4.2 Biasing

Application of an external bias to a Schottky diode can modify the depletion width and the potential drop across the junction [52]. Under forward bias, the potential drop across the depletion region is reduced, so the depletion width narrows and carrier transport is enhanced. Under reverse bias, the expanded depletion region increases the volume over which EHPs are generated and collected. Further, the electric field is stronger and enhances carrier drift velocity and reduces the probability that EHPs recombine and annihilate. The effect of applied bias on the band structure is illustrated in Figure 1.5.

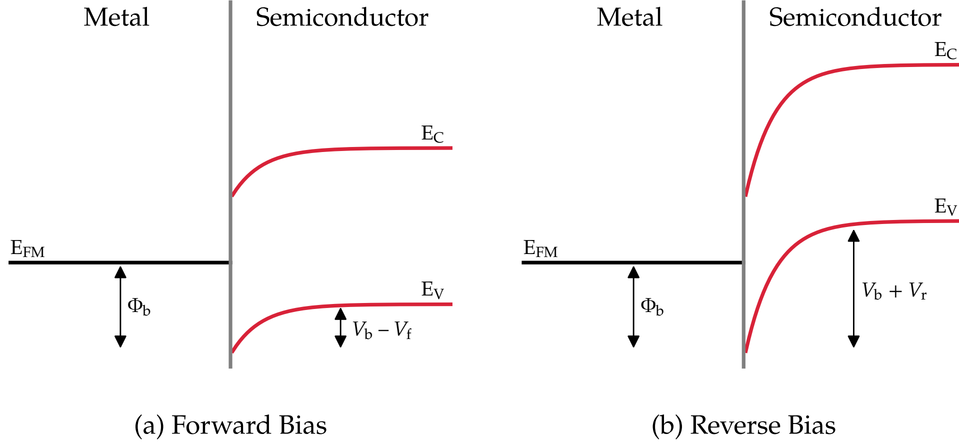

(a) Forward Bias (b) Reverse Bias

Figure 1.5: Energy band diagrams of a metal/p-type semiconductor Schottky junction under applied bias. (a) Forward bias reduces the effective barrier height by $V_b - V_f$, narrowing the depletion region and facilitating majority carrier transport across the interface. (b) Reverse bias increases the barrier to $V_b + V_r$, widening the depletion region and suppressing carrier flow. E_C and E_V denote the conduction and valence band edges, E_{FM} is the metal Fermi level, Φ_b is the Schottky barrier height, and V_b is the built-in potential.

1.4.3 Current–Voltage Characteristics

The current–voltage (I–V) characteristics of a Schottky diode reflect its rectifying behaviour (Figure 1.6), and in this work demonstrate the activity of a device under irradiation of beta particles. Under forward bias, current increases exponentially once the applied voltage sufficiently lowers the Schottky barrier, which increases carrier transport across the metal–semiconductor junction. This is defined as the forward voltage threshold. Although the current under reverse bias is ideally suppressed, in real devices the leakage current is still observed due to thermionic emission of carriers across the Schottky barrier, and the thermal generation of EHPs within the depletion region [52]. As the reverse bias increases, the electric field in the depletion region strengthens until it reaches the critical field of the semiconductor. At this point, carriers gain sufficient energy between collisions to generate additional EHPs by impact ionisation, causing a rapid increase in current. This process is known as avalanche breakdown, beyond which the device can no longer operate reliably.

The ratio of the forward current to the reverse current at the same magnitude of applied voltage is known as the rectification ratio, which indicates how effectively the diode conducts under forward bias while suppressing current under reverse bias. It is used in this work to provide a measure of the quality of rectifying behaviour.

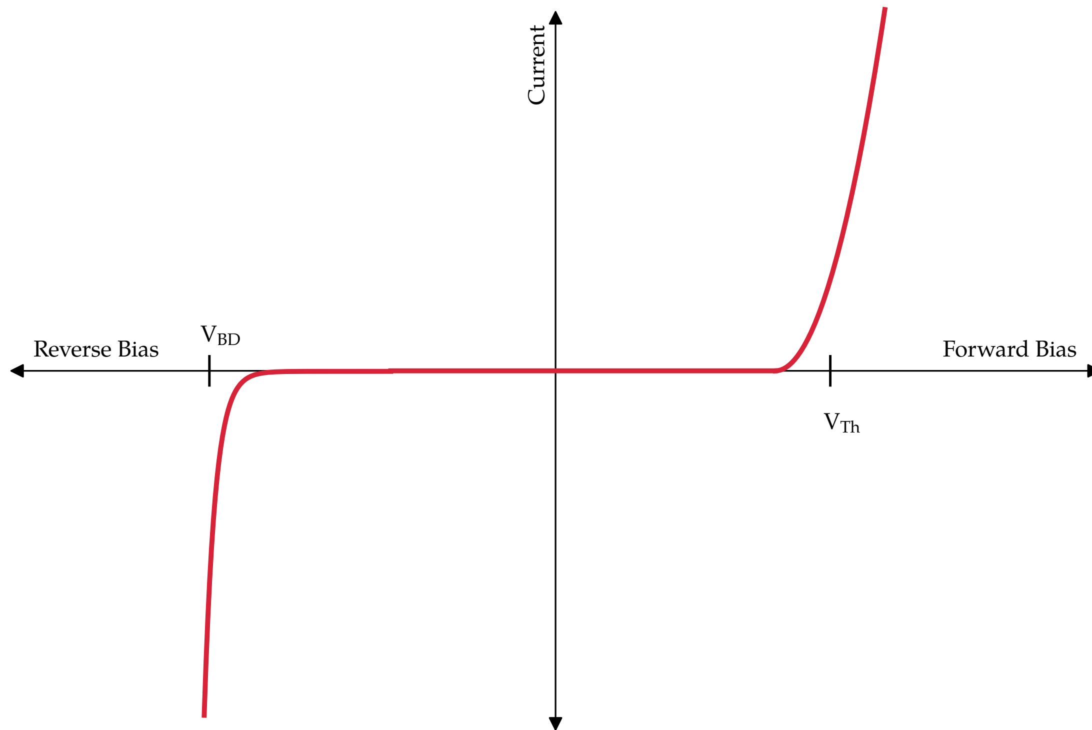

Figure 1.6: Idealised current–voltage (I–V) characteristics of a Schottky diode, illustrating rectifying behaviour. Under forward bias, the current increases exponentially once the applied voltage exceeds the threshold voltage, V_{Th}, due to reduction of the Schottky barrier and enhanced carrier transport. Under reverse bias, a small leakage current is present prior to breakdown, arising from thermionic emission and generation of electron–hole pairs (EHPs) within the depletion region. At sufficiently high reverse bias, the current increases sharply at the breakdown voltage, V_{BD}, due to avalanche breakdown.

1.5 Diamond

Although over 90% of modern electronic devices are fabricated from silicon (Si) [1], diamond displays properties that are important for low-energy beta detection, which are discussed below.

1.5.1 Properties

Table 1.2 summarises the key properties of Si, diamond, and other commonly used semiconductor materials [1]. With a band gap five times greater than Si, diamond more effectively suppresses thermally generated carriers, which improves the resolution of small charge signals associated with low-energy beta particles. A high breakdown field permits the application of strong electric fields without dielectric failure, increasing depletion width and thus EHP charge collection. Like GaAs, diamond has high carrier mobility, enabling rapid current response, but diamond has the added advantage that it is non-toxic [1]. Additional properties, such as high temperature tolerance, high saturated drift velocity, and moderate relative permittivity, indicate that diamond can support stable high-field device operation more effectively than conventional semiconductors.

This exceptional combination of properties identifies diamond as a promising semiconductor for low-noise, high-efficiency beta detection, motivating its investigation in this work. However, despite these advantages, challenges associated with material quality, defect density, and fabrication complexity have limited the widespread adoption of diamond devices.

Table 1.2: Key properties of common semiconductor materials [1].

	Si	**GaAs**	**SiC**	**GaN**	**Diamond**
Bandgap, E_G / eV	1.12	1.43	3.23	3.39	5.45
Thermal Conductivity, λ / W cm^{-1} K^{-1}	150	55	490	130	2200
Breakdown Voltage, E_C / 10^6 V cm^{-1}	0.3	0.4	3	3	10
Electron Mobility, μ_e / cm^2 V^{-1} s^{-1}	1500	8500	980	1250	1000
Hole Mobility, μ_h / cm^2 V^{-1} s^{-1}	480	400	100	200	2000
Relative Permittivity, ε_r	11.8	13.1	9.7	10.4	5.7
Saturated Drift Velocity / 10^7 cm^2 s^{-1}	1.0	2.0	2.0	2.2	1.1
Maximal Temperature, T_{max} / K	140	460	760	800	1350

1.5.2 Limitations of Diamond as a Semiconductor

Despite its exceptional intrinsic properties, the practical implementation of diamond-based devices remains constrained by small wafer size, historically challenging manufacture, and complexity with n-type doping.

High-quality, electronic-grade diamond wafers are only available in small wafer sizes, with production costs substantially higher than those of Si, SiC, and GaN [1]. Polycrystalline diamond offers a significant advantage due to its reduced cost as compared with single-crystal diamond; however, it contains grain boundaries and associated defect states that can act as charge trapping and recombination centres, degrading carrier transport and reducing charge collection efficiency in electronic applications. The extent to which these drawbacks hinder radiation detector performance remains insufficiently explored, which motivates the examination of this material for beta detection in this work.

Furthermore, whilst diamond synthesis has historically posed challenges, the advances in chemical vapour deposition (CVD) have enabling controlled growth of diamond films with tunable thickness, reduced porosity, and improved purity under comparatively moderate conditions [53, 54], and is therefore used in this work as the chosen method of diamond growth.

Finally, although p-type conductivity can be achieved through boron incorporation, controlled n-type doping presently remains a significant challenge. Although n-type doping has been achieved using nitrogen (N) to fabricate devices such as PIN diodes [55] and P–N diodes [56], limited reproducibility hinders the applicability of these structure. Accordingly, this work uses a Schottky diode

architecture, for which intrinsic or lightly p-type doped diamond is typically preferred [57–60].

1.6 Thesis Aims & Device Concept

The aim of this Thesis is to investigate whether a polycrystalline diamond Schottky diode can effectively detect and resolve low-energy beta particles, focusing on four representative beta-emitting isotopes — tritium, nickel-63, carbon-14, and promethium-147 — that are relevant to both radioisotope detection and betavoltaic applications. The intended design is shown in 1.7 and shows a metal–intrinsic–p-doped–metal (M–I–p^+–M) configuration. The p^+ is comprised of a BDD layer, that provides a suitable surface for metal deposition, enabling the formation of a low-resistance ohmic contact on diamond [2]. A thin membrane is incorporated into this architecture to minimise the distance travelled by EHPs before collection, thereby improving sensitivity to the small charge generation associated with low-energy beta particles, such as those emitted by tritium.

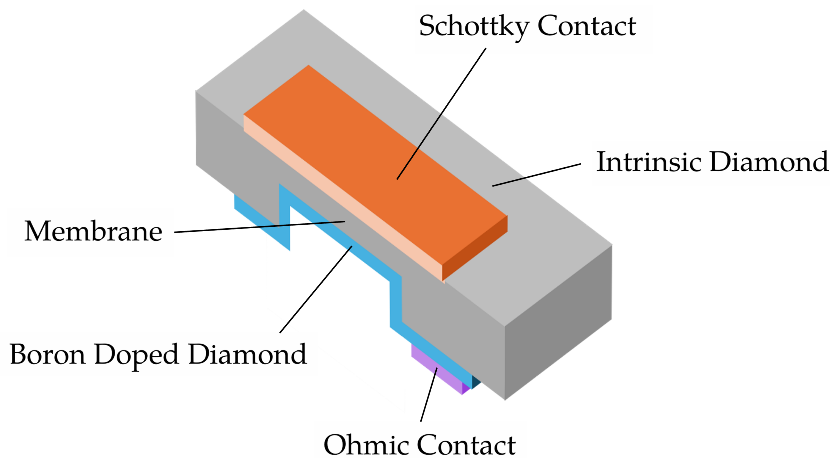

Figure 1.7: Schematic of the polycrystalline diamond Schottky diode structure fabricated in this work. From top to bottom, the device comprises a Schottky metal contact (orange), an intrinsic polycrystalline diamond layer containing a locally thinned membrane region (grey), a boron-doped diamond layer (blue), and an ohmic back contact (purple). The membrane is incorporated to enhance sensitivity to low-energy beta particles by reducing the charge carrier drift distance to the electrodes.

A secondary aim of this Thesis is to use CASINO simulations to optimise key parameters of the design, such as membrane thickness and Schottky metal type, and is discussed in Chapter 2. Subsequently, Chapter 3 describes device fabrication, Chapter 4 presents the characterisation of the device, and Chapter 5 evaluates device performance under simulated beta irradiation using an electron gun. Finally, Chapter 6 summarises the principal conclusions and outlines directions for future work.

Chapter 2: CASINO Simulations

2.1 Introduction

Developed in Canada at Sherbrooke University, the “monte **CA**rlo **SI**mulation of electro**N** trajectory in s**O**lids” software [61] is an excellent tool to simulate electron-matter interactions. The main objective of the program is the simulation of a complete electron trajectory through a material. CASINO assumes a Gaussian-shaped electron beam, where the user can specify the electron-beam diameter. Electrons are considered to have stopped interacting with matter once their energy has fallen below 50 eV. If the electron has escaped the surface of the sample, it is recorded as a backscattered electron. Thus, backscattering and penetration depth for a certain material can be found. Further, the energy by position distribution is a tool that displays the amount of energy lost by all the simulated electron trajectories a cross-sectional view of the energy absorbed in the sample, allowing the user to view the area of deposited energy in the cross section of the sample. Further detail is provided in Ref [61].

2.2 Simulation Parameters

The number of regions with different chemical composition and the thickness of each region were set to construct geometries for the desired simulation. These simulations included bulk diamond, bulk metals and part Al part diamond for the device model. The density used for each material are displayed in Table 2.1. The types of metals were chosen according to commonly used Schottky metals in literature [12]. After defining the material, the simulation was performed using the parameters listed in Table 2.2. Given the continuous energy distributions of beta particles, the representative energies listed in Table 2.3 were selected to approximate the average energy four low-energy beta-emitting radioisotopes considered in this work.

Table 2.1: Densities of the materials used in CASINO simulations.

Material	**Density / g cm^{-3}**
Diamond	3.52
Aluminium	2.70
Silver	10.49
Chromium	7.19
Gold	19.32
Platinum	21.45

Table 2.2: Parameters used in the CASINO simulation software.

Parameter	**Value**
No. simulated trajectories	100,000
Electron beam diameter / nm	1

Table 2.3: Representative energies of low-energy beta-emitting radioisotopes used for CASINO simulations.

Radioisotope	Representative energy / keV
Tritium	5
Nickel-63	20
Carbon-14	50
Promethium-147	60

2.3 Results & Discussion

2.3.1 Beta penetration depth

Table 2.4 summarises the maximum penetration depth, average penetration depth, and depth of maximum energy deposition for electrons incident on diamond across the simulated energy range. The depths increase with incident energy, reflecting the greater kinetic energy of the incident electrons which allows deeper penetration before complete energy loss.

For 5 keV incident energy electrons, a maximum penetration depth of 220 nm is reached, however their average penetration depth falls to just 130 nm, and strikingly, the maximum energy deposition is confined to within only 18 nm of the surface. Penetration depth increases with increasing incident energy, where by 60 keV electrons reach a maximum penetration depth of 19.7 μm, with the majority of energy deposition occurring at a depth of approximately 10 μm.

Thus, it is clear that the incident beta particle does not deposit its energy along its trajectory uniformly. The depth at which energy is deposited is critical, as it defines the region in which the majority of EHPs are generated, and thus a membrane should be kept as thin as possible to minimise the distance to the electrodes. However, this idea is balanced by the fact that if the membrane is too thin relative to the particle range, some electrons may pass through the device without depositing their full energy, causing the measured signal to underestimate the incident beta energy and reducing the ability to discriminate between different beta-emitting isotopes. As such, membrane thickness is optimised based on the maximum penetration depth to ensure full charge collection, although the depth distribution of energy deposition remains critical in determining where the signal is generated.

Table 2.4: Maximum and average penetration depths of simulated electrons in diamond at different incident energies.

Penetration depth / μm	5 keV	20 keV	50 keV	60 keV
Maximum	0.22	2.6	2.8	19.7
Average	0.13	1.7	8.2	12.1
Maximum energy deposition depth	0.13	1.7	8.2	12.1

Figure 2.1 visually demonstrates the paths taken by electrons as they traverse the diamond material. All trajectories exhibit lateral spread, which becomes substantially more pronounced at higher incident energies, increasing the likelihood of particle losses at the edges of the device which reduces charge collection efficiency. This effect may be minimised by larger-area substrates, which is more practically achieved with polycrystalline diamond than single crystal.

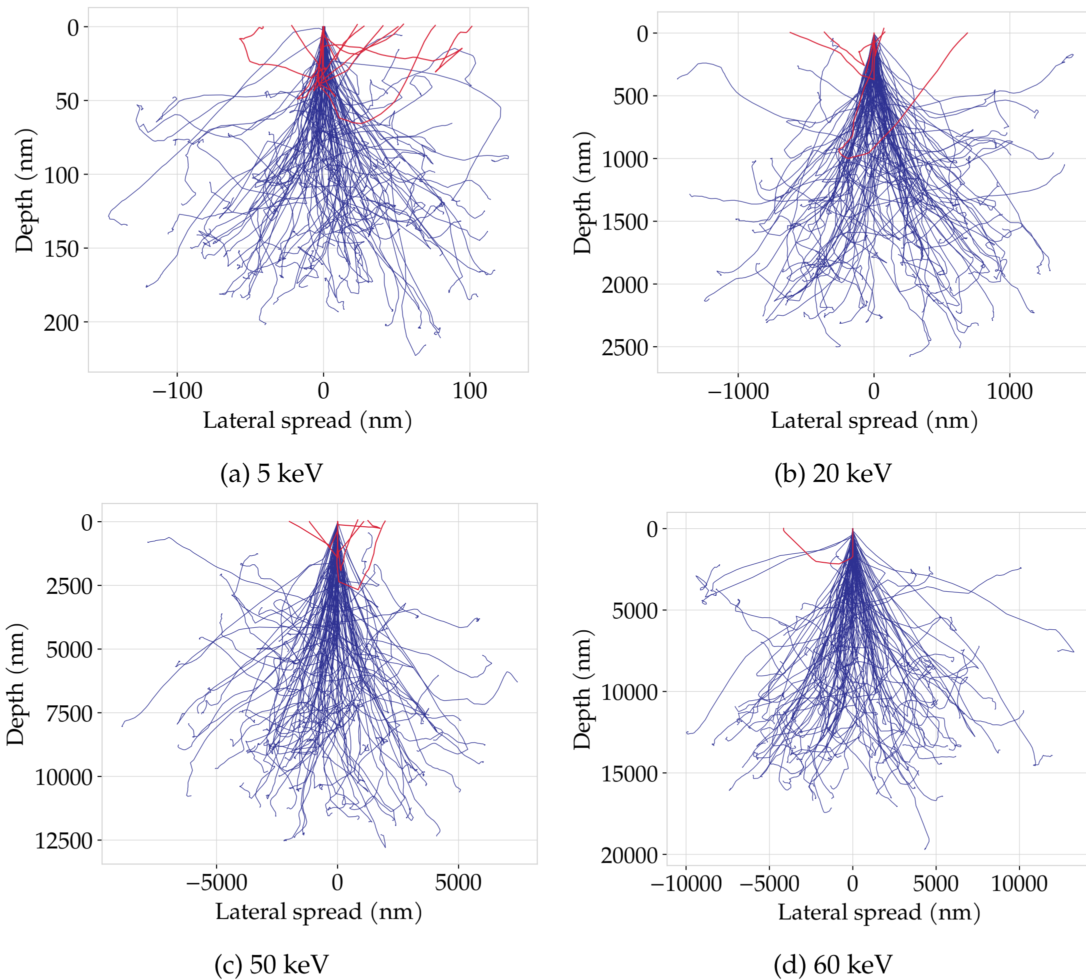

Figure 2.1: Simulated electron trajectories in diamond for increasing incident energies: (a) 5 keV, (b) 20 keV, (c) 50 keV, and (d) 60 keV. Higher energy electrons exhibit increased penetration depth and lateral spread, with more extensive scattering pathways. Incident trajectories are shown in red, while scattered electron paths within the diamond are shown in blue.

2.3.2 Backscattering

The beta-particle backscattering coefficient for various metals as a function of incident energy is shown in Figure 2.2. A clear dependence on atomic number is observed, with backscattering increasing from low-Z to high-Z materials, consistent with enhanced elastic scattering in heavier elements. Aluminium (Al) exhibits the lowest backscattering coefficient, with only 14% of incident electrons reflected. In contrast, high-Z metals such as gold and platinum reflect nearly half of the incident electrons (0.43% and 0.44% respectively), representing a signifi-

cant loss mechanism that reduces EHP generation within the diamond. The data highlights that low-Z metals favour particle transmission which may enhance signal generation.

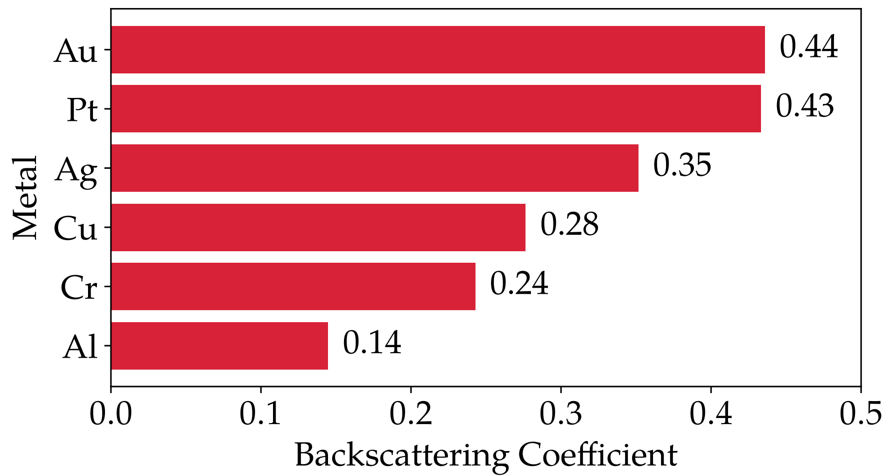

Figure 2.2: Backscattering coefficients of 5 keV beta particles for different metals. Higher atomic number metals (Au, Pt) exhibit significantly greater backscattering compared to lower atomic number materials such as Al, indicating reduced electron transmission into the diamond for high-Z contacts.

2.3.3 Schottky metal thickness

The region of energy deposition is shown in Figure 2.3 with different thickness of Al layers. The region where 90% of the beta particle energy is deposited is shaded red. 5 keV is used for all, since this is the energy that is most difficult to detect, and thus the most influenced by the top layer thickness. When the Al layer is below 35 nm, 90% energy is deposited in the diamond. This is good because this is the depletion region, and 90% energy will create the most carriers in the depletion region which will be swept and contribute to signal. However, above 35 nm thickness, 90% of the energy begins to deposit in the metal layer, and over 40 nm the entirety of 90% energy is deposited in the metal layer, where EHPs will not be swept and have reduced contribution to signal detection. This suggests that excessive metal thickness can degrade detector performance by displacing EHP generation away from regions where the electric field is strongest, highlighting the need for thin Schottky contact layers.

The region of energy deposition of 5 keV for varying Al thicknesses is shown in Figure 2.3, with the depth corresponding to 90% energy deposition highlighted in red. 5 keV was used because it represents the most challenging case for detection. As Al thickness increases from 10 to 22.5 nm, 90% of energy remains deposited just beneath the surface of diamond, ensuring that EHP generation occurs predominantly within the depletion region where carriers are efficiently collected. However, with increasing Al thickness this region shifts closer toward the metal, where beyond 40 nm 90% of energy is deposited in the metal itself. With the majority of EHP generation occurring outside the active region, charge collection is significantly reduced. As such, for an effective beta detector excessive metal thickness should be avoided as it may degrade detector performance.

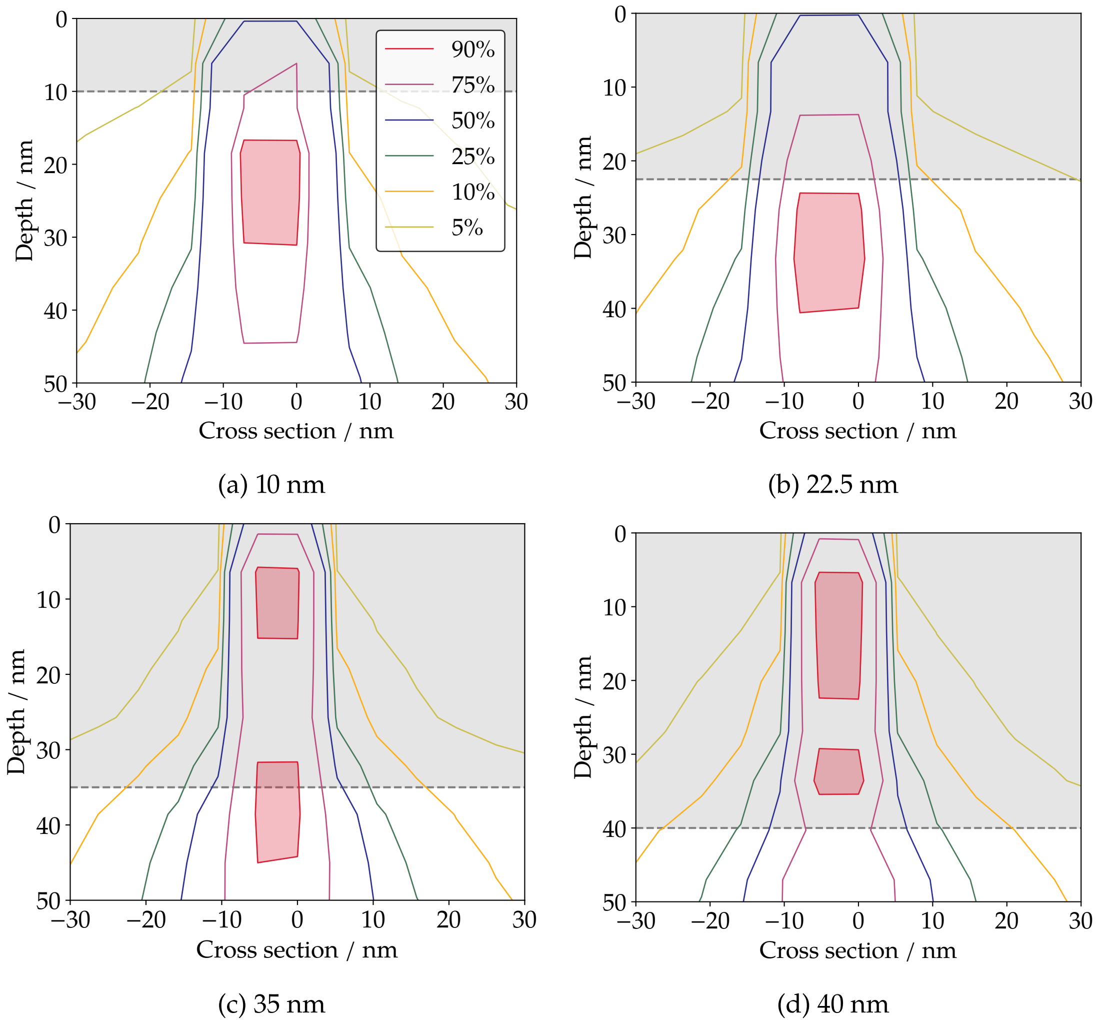

Figure 2.3: Energy deposition depth in diamond across varying aluminium thickness: (a) 10 nm; (b) 22.5 nm; (c) 35 nm; (d) 40 nm. The region where 90% energy is deposited is shown shaded region in red. The legend in (a) applies to all graphs.

2.4 Concluding Remarks

From the CASINO simulations, the following design criteria were identified for fabrication of the diode in this work:

(a) The membrane thickness should be above 19.2 μm in order to remain within the penetration range of beta particles emitted by 60 keV electrons, representative of Pm-147 radioisotope.

(b) Aluminium is a suitable choice of Schottky metal, as it exhibits a low backscattering coefficient at 0.14 and therefore minimises energy loss due to surface scattering effects at the metal contact.

(c) A 22.5 nm aluminium layer allows approximately 90% of the energy of 5 keV electrons to be deposited in the diamond, maximising EHP generation within the depletion region and improving the generated signal.

Chapter 3: Fabrication

3.1 Substrate Preparation

3.1.1 *Acid pre-treatment*

Free standing 10.0 × 10.0 mm PCD diamond substrates (product code: 145-500-0480) purchased from *Element Six, Ltd* (Ascot, UK) were immersed in a boiling mixture of concentrated sulfuric acid with potassium nitrate (6.5 g KNO_3 in 100 ml of 95% H_2SO_4 for 3h to remove residual contaminants from the polishing procedure.

3.1.2 *Laser cutting*

A 10.0 × 10.0 mm PCD diamond substrate was cut into four 3.3 × 6.7 mm PCD diamond substrates using a diode-pumped nanosecond laser (Nd:YAG) with a wavelength of 532 nm (Alpha 532, Oxford Lasers Ltd.). The dimensions were chosen to match those of SCD substrates used in other works which enabled shared use of equipment required at later stages (Section 3.3.3).

Figure 3.1: Photograph of the Oxford Lasers Alpha 532 laser micromachining system used to cut and etch the diamond substrate using programmed scan templates.

3.2 Diamond Membrane

3.2.1 Laser etching

To fabricate a thin membrane into the substrate, a 2.5 mm × 1.0 mm lozenge-shaped membrane was constructed in Cimita (Figure 3.2). A cross-hatch scanning pattern was included to maximise material removal and minimise surface roughness generated by repeated exposure to parallel laser lines.

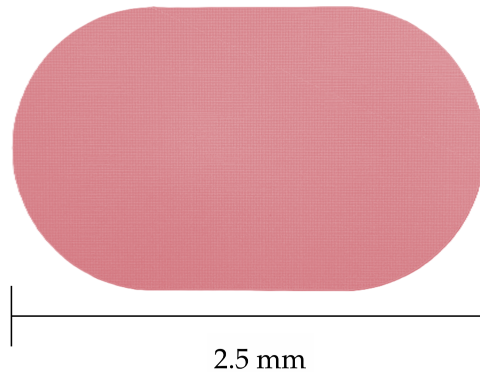

Figure 3.2: Representation of the laser scan template used in Cimita software for membrane fabrication, showing a cross-hatched rastering pattern to maximise uniform material removal.

To etch the substrate, the stage was positioned 31.5 mm from the laser incidence point along the z-axis (which enabled high laser focus), the power was set to 25% and a velocity of 2 (units?) was chosen. A focused laser beam dissipated the power to a small area, and low velocity increases contact time between the laser and the substrate surface. This generated the necessary thermal energy to induce a phase transition from diamond to graphite. These conditions were sufficient to vaporise the top graphitic layer while inducing the formation of a new underlying graphite layer within the same etch pass. The substrates were then sonicated to remove loosely bound graphite from the substrate surface. Membrane thickness following each pass was measured using the LEXT Optical Microscope. Each time 50 µm of material was removed, the scan template was reduced in size by 5% to produce a stepwise sidewall profile to reduce strain. This step was necessary as strain within the diamond otherwise results in mechanical fracture of the membrane.

Table 3.1: Laser machining parameters used for membrane fabrication.

Parameter	$> 50\,\mu m$	$< 50\,\mu m$	Graphite Removal
Power %	25	10	10
Z-axis	31.5	31.5	31.3
Etch speed	2	2	3
Index speed	15	15	15
Etch passes	1	1	1
Sonication time / minutes	3	1	1
Repeats	20	10	20

This process was repeated until the membrane reached >50 µm, at which point the power was reduced to 10% and the velocity was increased to 3 (machine units). The higher speed reduced the time spent per unit area, reducing thermal contact time and therefore shortening the interaction length. This leads to shallower microgrooves which increases surface smoothing. Following each etch pass, another set of conditions termed 'Graphite Removal' were used. Laser focus was reduced to 31.3 mm to allow the thermal energy to dissipate over a larger area, providing insufficient energy for the phase transition, but sufficient energy for graphite vaporisation, which removed the surface graphitic layer but preserved the diamond underneath. This was performed prior to LEXT measurements as incorporation of the surface graphite layer woule lead to over estimation of the membrane thickness. Once the two conditions were applied in sequence, the substrates were sonicated and characteristed via LEXT. These steps were repeated until the membrane reached 35 microns, at which point 5 passes of 'graphite removal' were performed to smoothen and partially clean the surface prior to subsequent processing steps. The laser treatment parameters are summarised in Table 3.1.

3.2.1.1 Sonication

Prior to sonication the substrate was placed in a 50 ml beaker containing 30 ml iPa solution, before securing to a clamp stand. Once set up, the sonicator was turned on and left to sonicate for the period of time listed in table 3.1, which was shorter for thinner membranes to reflect their increased fragility. Sound waves propagating through the liquid medium induce vibrations in the device and force out the contaminants from areas inaccessible with a cotton bud or brush.

3.2.2 H-plasma CVD

Reduction of laser micromachining grooves (microgrooves) and further removal of graphite was achieved via exposure to hydrogen plasma (H-plasma) which preferentially etched graphitic carbon over diamond. An Applied Science and Technology (ASTeX)-type microwave plasma-assisted chemical vapour deposition (MW-CVD) reactor was used and is shown in Figure 3.3. In brief, a 1.5 kW

magnetron generated microwaves with a frequency of 2.45 GHz and ionised reaction gases in the chamber to result in plasma formation in a ball directly above the substrate. Radicals diffuse from the plasma ball to the substrate and initiate a series of reactions, dependent on the types and ratios of the gases present. A full description of the operating principles can be found in Ref [62].

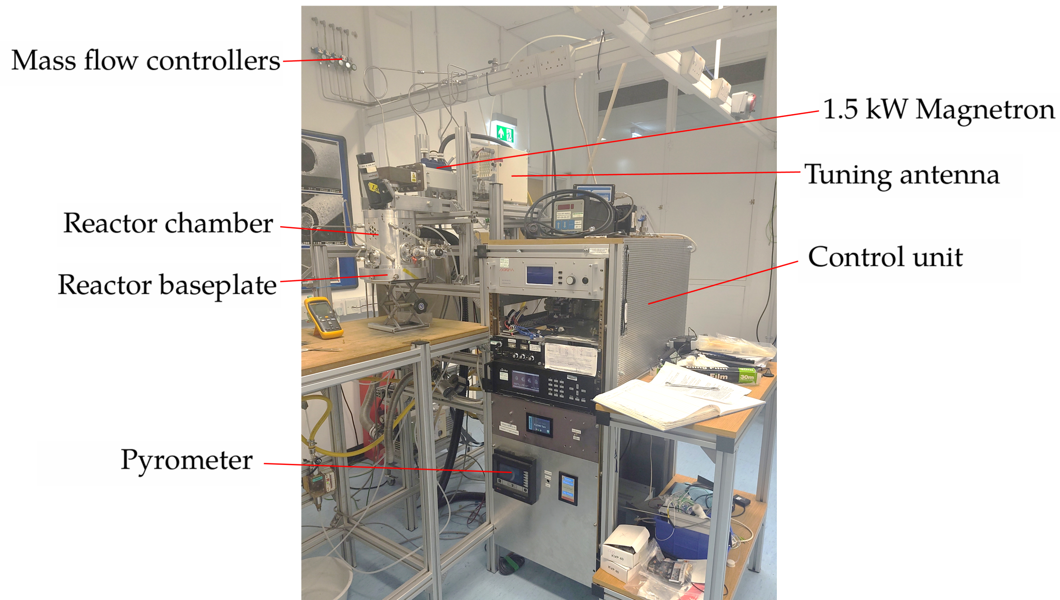

Figure 3.3: Photograph of the Microwave plasma chemical vapour (MW-CVD) Astek type reactor used for undoped diamond growth, with key components indicated.

The substrates were mounted onto a molybdenumm disk placed on top of a Mo spiralled wire with a diameter of 8 mI on the reactor baseplate. The purpose Mo spacer wire was to lower the thermal contact between the W disk and the water-cooled baseplate so that the substrate may reach the higher temperatures required for CVD. Upon loading the sample, ambient gases were removed from the chamber by pumping down to 0.2 Torr. H_2 gas (300 sccm), regulated by a mass flow controller, was introduced into the chamber and a plasma struck at 15 Torr using 0.65 kW microwave power. Once struck, the pressure and power were promptly increased to 130 Torr and 1.3 kW respectively so as to introduce space between the plasma and substrate. This reduced electron bombardment to the substrate. The reflective power was tuned to 0 kW *via* linear tuning antenna at the top of the CVD reactor. The plasma ball remained localised directly above the sample at the center of the chamber for the duration of the run. The substrate temperature was measured as 950°C using a single-colour optical pyrometer set to 0.15 emissivity corresponding to a PCD substrate. At the start of the treatment, the substrate glowed orange which was indicative of non-diamond carbon removal. The orange glow stopped after 15 minutes, indicating fewer graphitic impurities were present, and so marked the end of the treatment. Photographs of the substrates during the CVD process are shown in Figure 3.4.

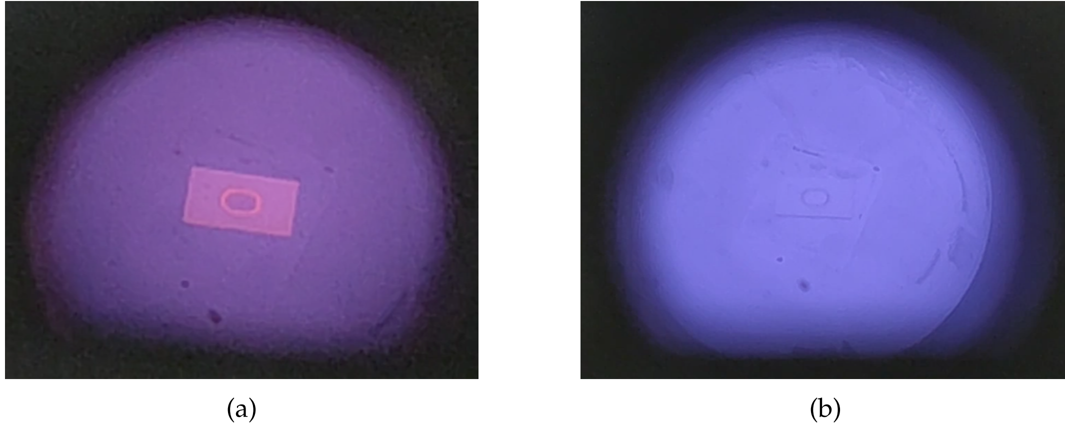

(a) (b)

Figure 3.4: Photograph of the substrate inside the undoped MW-CVD reactor during (a) start and (b) end of H-plasma treatment.

After 15 minutes, the pressure was reduced to 30 Torr and power was simultaneously reduced until the plasma disappeared at 0.22 kW and the power generator was set to standby. H_2 gas was allowed to flow over the sample for 2 minutes at 30 Torr and 0 kW to cool the substrate. The following shutdown procedure was performed; the pressure was set to 0 Torr, gases were switched off, and the chamber was evacuated of all gases before unloading and retrieving the substrates. The etch parameters for this procedure are summarised in Table 3.2.

Table 3.2: Hydrogen plasma CVD parameters for graphite etching.

Parameter	Value
H_2 flow / sccm	300
Power / kW	120
Pressure / Torr	120
Temperature / °C	1030
Time / minutes	90
Pyrometer emissivity	0.18
Wire / mI	8

3.3 Ohmic Contact

3.3.1 Boron Doped Diamond CVD

Growth of a conductive BDD layer accomplished using a bespoke (ASTeX)-type MW-CVD reactor shown in Figure 3.5 which is exclusively used for boron doped CVD. The operating principles described in section 3.2.2 for the pure (ASTeX)-type MW-CVD reactor apply to the boron CVD reactor, with the important distinction that the latter contains residual boron impurities within the chamber, making it unsuitable for pure diamond or H-plasma CVD but applicable for

BDD growth.

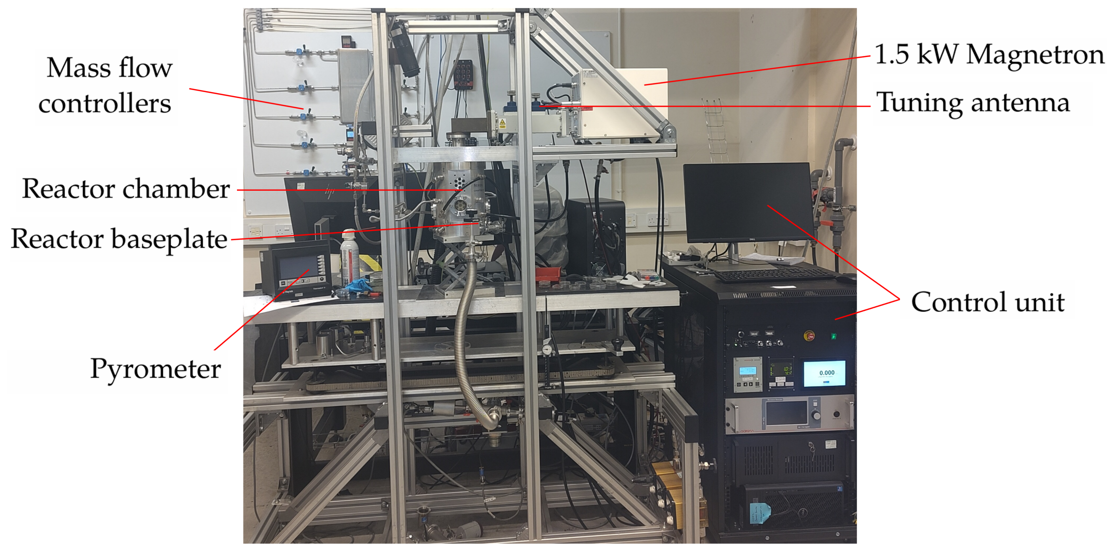

Figure 3.5: Photograph of the Microwave plasma chemical vapour (MW-CVD) Astek type reactor used for boron-doped diamond growth, with key components indicated.

With the etched membrane facing upward, the substrates were mounted onto a molybdenum disk and covered with a bespoke molybdenum mask as shown in Figure 3.6 which specified the area of BDD growth. The mask and disk were in contact with for unobstructed thermal conduction. This setup was loaded onto a Mo spacer wire with a diameter of 8 mI aligned centrally in reactor baseplate.

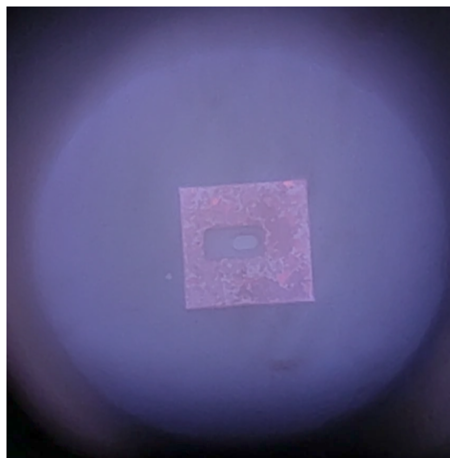

Figure 3.6: Photograph of masked boron doped diamond MW-CVD growth

Upon loading the sample, ambient gases were removed from the chamber by pumping down to 0.2 Torr, then H_2 gas (300 sccm) regulated by a mass flow controller was introduced into the chamber and a plasma struck at 15 Torr and 0.65 kW microwave power. Once struck, the pressure was promptly increased to 50 Torr and CH_4 gas (12.5 sccm) was introduced. This prevented etching of

the substrate by the H_2 gas and present boron impurities. The plasma changed colour from purple to pale green, indicating the presence of 'swan band' transitions characteristic of the carbon dimer radical. In quick succession, the pressure and power were increased to 120 Torr and 1.2 kW respectively, B_2H_6 (0.6 sccm) was added to the chamber, and the reflective power was tuned to 0 kW. The plasma ball remained stable and localised directly above the sample throughout the run. With the mask on the outer surface of the substrate, the emissitivty of the single-colour optical pyrometer (= 2.2 µm) was set to 0.18 corresponding to molybdenum. The power and pressure were marginally adjusted throughout the run to maintain a temperature of 1030°C. This is expected to be higher than the actual temperature of diamond substrate beneath due to the different thermal properties of the materials. The growth deposition time was 90 minutes, after which the substrates were cooled at a pressure and power of 30 Torr and 0 kW for 2 min, before initiating shutdown procedure as described in section 3.2.2. The BDD growth parameters are summarised in Table 3.3.

Table 3.3: CVD parameters for boron doped diamond growth.

Parameter	Value
H_2 flow / sccm	300
CH_4 flow / sccm	12.5
B_2H_6 flow / sccm	0.6
Power / kW	120
Pressure / Torr	120
Temperature / °C	1030
Time / minutes	90
Pyrometer emissivity	0.18
Wire / mI	8

3.3.2 H-termination

Although boron CVD yields H-terminated substrates, boron impurities accumulate at grain boundaries in PCD diamond materials (ref) and thus the surface coverage is not pure or uniform which hinders metal adhesion performed in subsequent steps (section 3.3.3). For this reason, the H-termination was amended in the MP-CVD reactor (Figure 3.3, section 3.2.2) which followed a three step process, with each step lasting 2 minutes. Firstly, existing terminations desorbed from the surface under high pressure and power of 90 Torr and 0.90 kW respectively. Secondly, the diffusion distance between the plasma and substrate was minimised to facilitate termination. The pressure was decreased to 50 Torr to lower the plasma ball toward the substrate. The power was reduced to 0.75 kW to minimise etching and electron bombardment. Finally, to avoid replacement of H by atmospheric oxygen, the substrates were cooled under H_2 gas flow over a power and pressure of 30 Torr and 0 kW respectively. The H-termination param-

eters are summarised in Table 3.2.

Table 3.4: Hydrogen plasma CVD parameters for H-termination.

Parameter	Desorption	Termination	Cooling
H_2 flow / sccm	300	300	300
Power / kW	120	75	0
Pressure / Torr	120	50	30
Temperature / °C	900	750	n/a
Time / minutes	3	3	3
Pyrometer emissivity	0.15	0.15	0.15
Wire / mI	8	8	8

3.3.3 *Pt/Pd Metal Deposition*

The freshly H-terminated substrates were enclosed within a shadow mask shown in Figure 3.7(a) that selectively exposed the BDD surface area for metallisation.

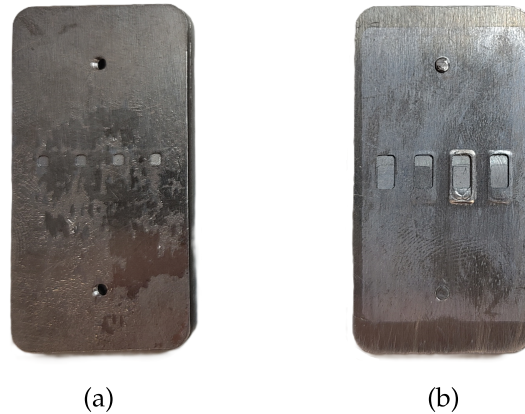

(a) (b)

Figure 3.7: Shadow masks used for metallisation: (a) Pt/Pd deposition mask and (b) Al deposition mask.

Pt/Pd contacts were deposited onto the exposed region using a high-resolution sputter coater (AGAR Scientific, AGB7234) (Figure 3.8). The shadow mask containing the substrate was positioned at the base of the chamber and a Pt/Pd target was placed into the target holder. The chamber was evacuated to a base pressure of 10^{-5} mbar, the deposition time was set to 120 s, and the process was initiated. Argon gas entering the chamber ionised to form a plasma through application of a high voltage which established the metal target as the cathode. Positive argon ions bombarded the target surface and ejected metal atoms that deposited onto the interior chamber walls and thus coated the exposed regions of the substrate.

Figure 3.8: Photograph of the AGAR Scientific sputter coater used for Pt/Pd deposition, with key controls indicated.

3.4 Schottky Contact

3.4.1 O-termination

Oxygenated surfaces were obtained using an UVO-cleaner kit (Model 42, Jelight Company Inc.). A mercury lamp stationed 4 cm above the samples generated UV light, which supplied photons of 184.9 nm as a source of energy for the conversion of atmospheric oxygen into ozone under room temperature and pressure. Upon the absorption of 253.7 nm photon wavelengths, the ozone molecule decomposed into the oxygen radical and oxygen dimer. The oxygen radical reacted with the surface of the substrate to replace prior termination with oxygen containing surface groups, the specificity of which is discussed in Ref. Both sides of the substrate were exposed for 35 minutes. Termination of both faces ensured that no H-termination was present surrounding the edges which would result in the short circuit of the device during later testing procedures.

Figure 3.9: Photograph of the Jelight 42 UVO-cleaner equipment used for oxygen termination, with key components indicated.

3.4.2 *Al Deposition*

The O-terminated substrates were placed inside the shadow mask shown in Figure 3.7 (b) with a the large exposed area directly above the membrane. 22.5 nm of Al was deposited by Prof. Neil Fox using the Balzer system in physics.

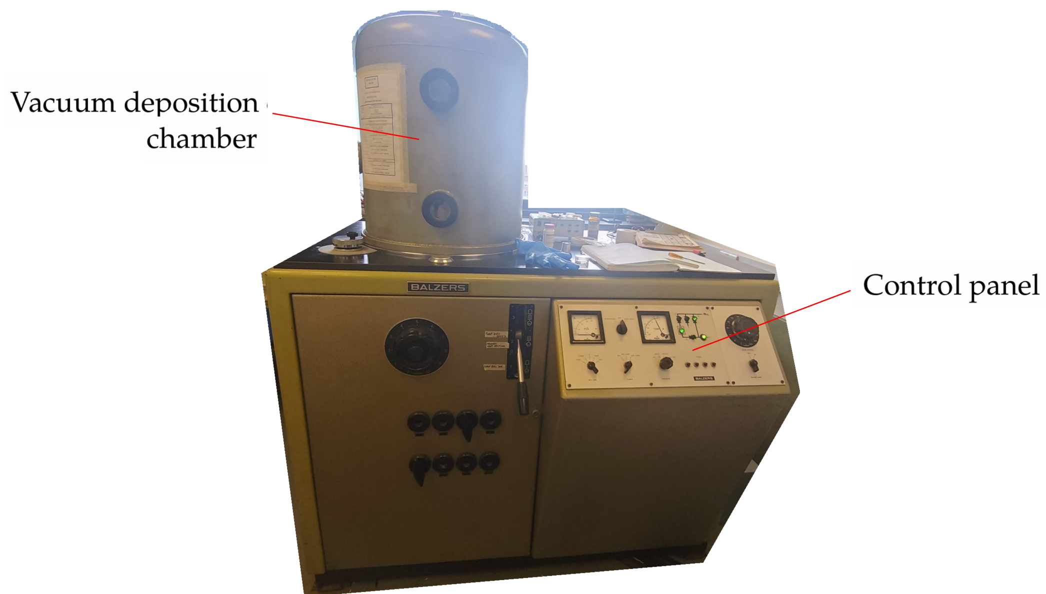

Figure 3.10: Photograph of the Baltzer system in physics used by Prof. Neil Fox to deposit 22.5 nm of aluminium onto the sample for the formation of the Schottky contact.

Chapter 4: Characterisation

4.1 LEXT

4.1.1 *Overview*

The LEXT OLS5100 microscope is a laser scanning confocal optical system that enables high-definition imaging and three-dimensional surface characterisation [63]. It employs a 405 nm laser source and a confocal optical configuration, in which only light passing through a circular pinhole at the focal plane is detected, while out-of-focus and scattered light is rejected. This significantly reduces blur and enhances image contrast compared to conventional optical microscopy . Height information is obtained by acquiring a series of confocal images at different focal positions along the z-axis. For each pixel, the detected light intensity as a function of focus position forms an intensity–depth curve. By combining the peak intensity data across all pixels, an image is produced in which the entire surface appears in focus. The accumulation of peak positions enables reconstruction of the sample's three-dimensional topography. For samples exceeding the field of view, multiple scans can be stitched together to generate a larger composite image.

4.1.2 *Data Acquisition*

The device was placed onto a glass slide, which was cleaned with isopropanol (IPA) and positioned at the centre of the LEXT stage. A 20 x objective was used for all measurements. A map of the sample was obtained and saved as an image. A stitched scan area was selected to cover the full sample. The vertical scan range was defined by setting the minimum height at the stage surface and the maximum at the sample surface. The room lights were switched off, and the scan was performed over the course of approximately 45 minutes to produce three-dimensional surface data.

During data processing, noise was reduced using the "fill in using neighbours" method, and sample tilt was corrected using the "specify the plane defined 3 points or more" method that defined the glass slide as a flat reference plane. Cross-sectional profiles were extracted using the "depth profile" tool and exported for further analysis.

4.1.3 *Results & Discussion*

4.1.3.1 LEXT Images

Figure 4.1(a) shows an optical image of the completed device, and the relative positions of the membrane, intrinsic diamond, boron-doped diamond, Pt/Pd ohmic contact, and Al Schottky contact. The final outcome of the fabrication process is in accordance with the intended design illustrated in Figure 1.7. The

corresponding three-dimensional depth image is shown in Figure 4.1(b), where the membrane topography is visualised using a colour scale to represent height variation.

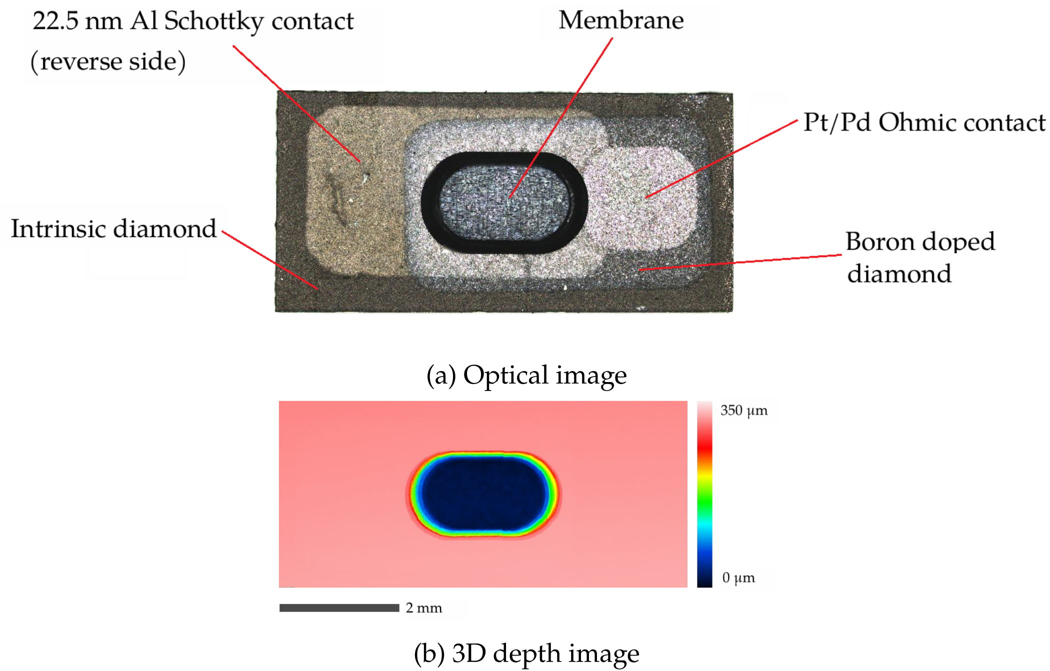

(a) Optical image

(b) 3D depth image

Figure 4.1: Completed polycrystalline diamond device. (a) Optical image showing the membrane region, intrinsic diamond, boron-doped diamond, Pt/Pd ohmic contact, and the 22.5 nm Al Schottky contact on the reverse side. (b) Three-dimensional depth image of the membrane region, with the colour scale indicating surface height.

4.1.3.2 Cross-Section Depth Profile

Figure 4.2 shows that the total substrate thickness was approximately 330 µm. Laser processing removed about 297 µm of material, leaving a membrane thickness of approximately 33 µm. This thickness lies within the range predicted by CASINO simulations to effectively capture the energy deposited by Pm-147 beta particles. The membrane sidewalls exhibit a gradual slope with distinct step-like features, corresponding to transitions between successive template sizes during laser machining.

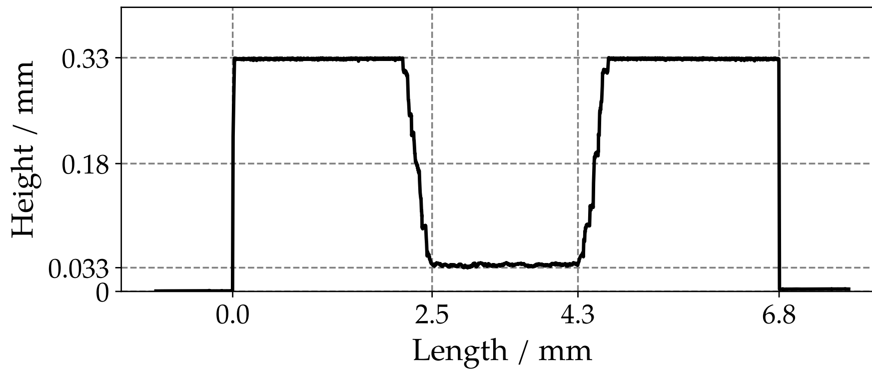

Figure 4.2: The cross section depth profile of the diamond membrane, indicating a final thickness of 33 μm.

4.2 Raman

4.2.1 Overview

Raman spectroscopy is a non-destructive technique that uses laser excitation to characterise crystalline structure, bonding type, identify atoms and impurities [64–66].

Raman peak positions reflect the vibrational energies of the system, as determined by the energy shift during inelastic scattering. Photons from the laser carry an oscillating electric field, which can distort the electron cloud within the material. A dipole moment is induced through redistribution of charge, and if a vibrational mode changes the polarisability of the electron cloud, then it will oscillate at a frequency different from that of the incident light. This inelastic form of scattering is known as Raman scattering, where the shift in energy determines the position of the peak and is characteristic of the species present in the sample. In contrast, oscillations of the same frequency as incident light do not appear as shifted features in the Raman spectrum; this scattering is elastic and known as Rayleigh scattering. Further detail can be found in Ref [66].

The full width at half maximum (FWHM) of the peak is associated with crystalline quality [64, 67, 68]. High-quality crystals produce narrow peaks and small FWHM because the regular lattice vibrates uniformly, causing the induced dipole to oscillate at a well-defined frequency. Disorder, defects, and strain introduce variations in local environments within the lattice, each oscillating at a slightly different frequency, thus broadening the distribution of Raman shifts and increasing the FWHM.

Whilst absolute intensity is influenced by experimental conditions, ratios of peaks within a spectrum highlight the relative contributions of different structures or bonding environments. Independent of measurement conditions, they provide insight into relative phase content and assess the degree of disorder in the material [69, 70].

4.2.2 *Data Acquisition*

All Raman spectra were recorded in air and at room temperature in backscattering geometry using a Renishaw 2000 Raman spectrometer. A tunable Ar ion laser was used as an excitation source to produce a 532 nm (green) laser. The spectral range center was set to 1332. Spectra were recorded over 10 accumulations with 10 s exposure time at 50% laser power. The Raman scattering spectra were investigated in the spectral range of 600 to 2000 cm^{-1}. All data collection were analysed using Renishaw WiRE 2.0 software by curve fitting method, applying a mix of Lorentzian and Gaussian functions. Data were processed and presented using python.

4.2.3 *Results & Discussion*

4.2.3.1 BDD

An prominent peak at 1332 cm^{-1} was observed both before and after BDD growth and is identical to that stated in the literature for diamond [64]. The absence of additional peaks in the spectra indicates a high degree of crystalline quality in the substrate, as no features associated with sp^2 hybridisation are observed despite the polycrystalline nature of the substrate. However, the absence of characteristic boron-related features in the doped sample is unexpected. Literature reports that BDD exhibits a broad peak between 1200 and 1280 cm^{-1} [71], as well as asymmetry in the diamond peak due to Fano resonance [72, 73] or a blue shift associated with lattice distortion and tensile stress [74]. The lack of these features in the BDD spectrum may indicate that the BDD layer is substantially thin, so that the underlying diamond substrate has dominated the spectrum and masked signatures of boron incorporation [75].

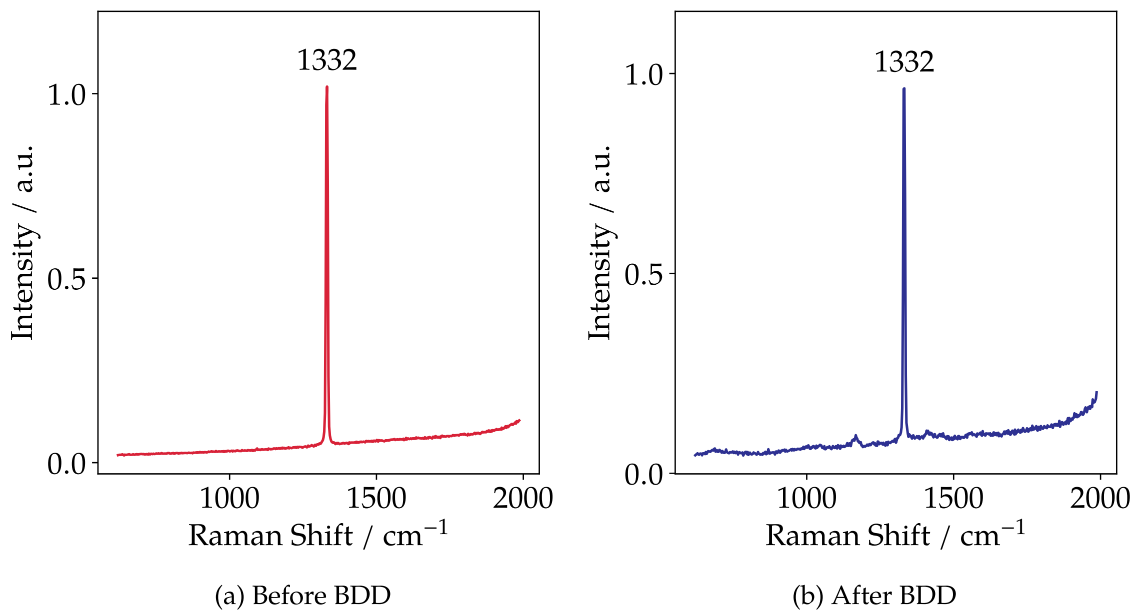

Figure 4.3: Raman spectra of the membrane surface (a) before and (b) after boron-doped diamond (BDD) growth. In both cases, a sharp peak at 1332 cm^{-1} is observed, corresponding to the first-order diamond Raman mode.

The FWHM of single crystal diamond is approximately 1.2 cm^{-1} [64], whereas the undoped substrate exhibits a broader value of 7.9 cm^{-1}. The broadening is expected, since the substrate is polycrystalline thus inherently contains more structural disorder and a range of local environments, leading to a distribution of Raman shifts. Following BDD growth, the FWHM increases marginally by 0.2 cm^{-1}, suggesting a small increase in disorder, defects, or lattice strain, which has been recorded with boron incorporation into the diamond lattice [71].

Table 4.1: Centre position and full width at half maximum (FWHM) of the diamond Raman peak before and after BDD growth. The small increase in FWHM after BDD growth suggests a marginal increase in disorder, defect density, or lattice strain.

Sample	**Peak / cm^{-1}**	**FWHM / cm^{-1}**
Pre BDD	1331.75	7.92
Post BDD	1332.25	8.12

4.2.3.2 Laser Treatment

The **G** peak, associated with crystalline **g**raphite [65, 75], is typically observed between 1500 and 1600 cm^{-1} [64, 76, 77]. In the spectrum, the peak at 1575 cm^{-1} corresponds to the G band and is an exact match for that found in literature [75, 78], with Dychalska et al. describing this feature as highly ordered pyrolytic graphite [65]. The **D** peak arises from **d**isordered graphite and is observed between 1320 and 1360 cm^{-1} [64, 76, 77]. The observed peak at 1355 cm^{-1} corresponds to the D band and identically matches that reported in literature [65, 79]. This feature has been associated with micro- or nano-crystalline diamond and disordered carbon phases [80]. Additional peaks have been observed in nanocrystalline and highly disordered materials, as reduced crystallite size and loss of long-range order allow more vibrational modes to become Raman active [66]. The peaks at 784 and 944 cm^{-1} may therefore arise from lattice distortions or defect-related vibrational modes. For example, sp^2 out-of-plane bending modes have been reported around 750 cm^{-1} [80].

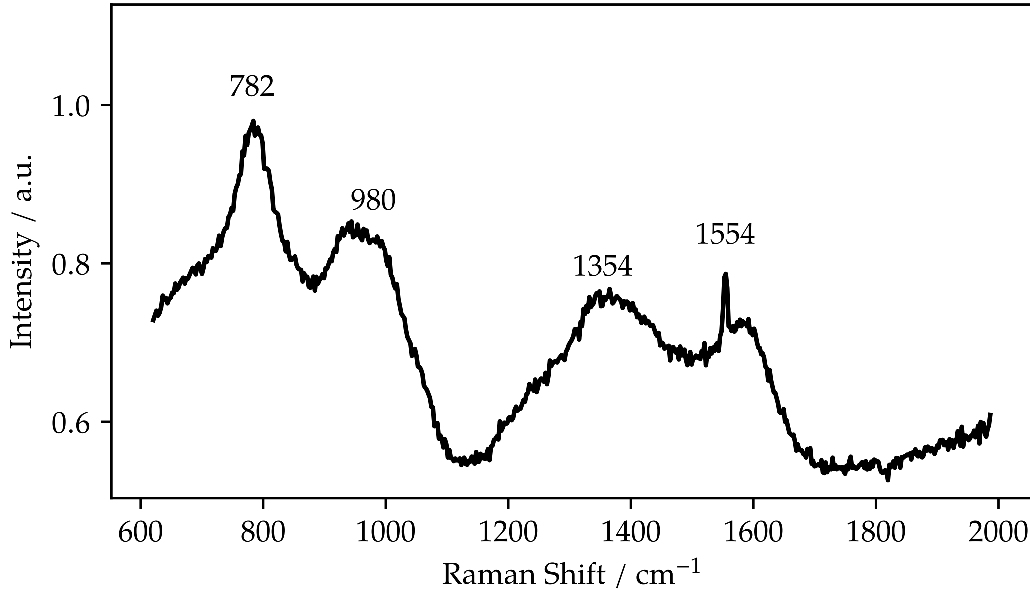

Figure 4.4: Raman spectrum of the laser-treated membrane surface prior to BDD growth. Bands at 1354 and 1554 cm^{-1} correspond to the D and G bands respectively, indicating the formation of sp^2-bonded carbon. Broad features at 782 and 980 cm^{-1} are associated with amorphous or nano-carbon phases.

The FWHM values are significantly broadened, indicating a high degree of structural disorder and a wide distribution of vibrational environments. The largest broadening is observed for the D band at 1354 cm^{-1}, consistent with substantial disorder within the sp^2 carbon phase. This is consistent with the ratio of the D to G peaks at 0.87, placing the material in the nanocrystalline to moderately disordered regime. This aligns with laser-induced graphitisation, where small, defective graphitic clusters are formed rather than well-ordered graphite [69].

Table 4.2: Peak positions and full width at half maximum (FWHM) values obtained from the Raman spectrum of the laser-treated membrane surface prior to BDD growth. The broad linewidths indicate a high degree of structural disorder and a distribution of non-diamond carbon phases across the surface.

Peak / cm^{-1}	**FWHM / cm^{-1}**
782	64.4
980	110.8
1354	162.7
1554	68.9

4.3 SEM

4.3.1 Overview

Scanning Electron Microscopy (SEM) is a high-resolution imaging technique that uses a focused beam of electrons to probe the surface of a sample, and provides

significantly greater spatial resolution than optical microscopy.

When the electron beam interacts with the material, incident electrons undergo elastic scattering (producing backscattered electrons) and inelastic scattering (producing secondary electrons and characteristic X-rays) to generate signals providing information. Of these, secondary electrons significantly contribute towards the generation of high-resolution imaging of surface features. As the electron beam is scanned point-by-point across the surface in a raster pattern by electromagnetic coils, a detector collects these electrons at each beam position and converts their intensity into pixel brightness, producing an image where brighter regions correspond to areas emitting more SE. Because SE originate from only the top few nanometres, SEM images predominantly represent surface topography, with features such as edges and grain boundaries appearing enhanced due to increased electron emission.

4.3.2 Data Acquisition

Carbon tape was placed on a circular disk. Using fine tip plastic tweezers, the sample was carefully and precisely placed on the centre, with the etched membrane facing upwards. Gentle pressure was applied around the edges of the chip using flat plastic tweezers to ensure uniform adhesion, avoiding direct contact with the membrane. Ensuring full adhesion prevents unadhered regions from lifting relative to the adhered regions, which may result in fracture. The mounted sample was placed inside a JSM-IT300 SEM kit from JEOL and placed under vacuum. A working distance of 10.8 mm, probe current of 30 A and electron acceleration voltage of 30.0 kV were used to acquire images.

To dissolve the carbon tape, the ensemble was placed into a 50 ml beaker and fully immersed in acetone for 10 minutes. Plastic tweezers were then used to gently nudge the edges of the chip, applying as little pressure as possible, and whilst ensuring it remained fully wetted with acetone, until the chip slid off the tape.

4.3.3 Results & Discussion

4.3.3.1 After Laser Treatment and H-Plasma CVD

The SEM images acquired following membrane fabrication are shown in Figure 4.5. Across the periphery of the membrane surface, the mild microgroove morphology is observed which is characteristic of the laser scanning process. In contrast, the central membrane surface retains a well-defined polycrystalline grain structure, indicating minimal laser-induced damage during laser etching. This suggests that the combination of low power laser treatment and H-plasma CVD treatment is most effective in the central region. H-plasma CVD treatment at the membrane periphery is may be hindered by the surrounding membrane walls, which limit plasma accessibility to these regions.

The membrane walls appear bright due to enhanced secondary electron emis-

sion from steep features inclined toward the detector. The stepped profile arising from sequential laser templates is clearly resolved. They may impede carrier transport, which may limit the number of EHPs reaching the electrodes. Clear microgrooves are observed, indicating that neither reduced-power laser processing nor subsequent H-plasma CVD treatment was effective on highly inclined or vertical surfaces.

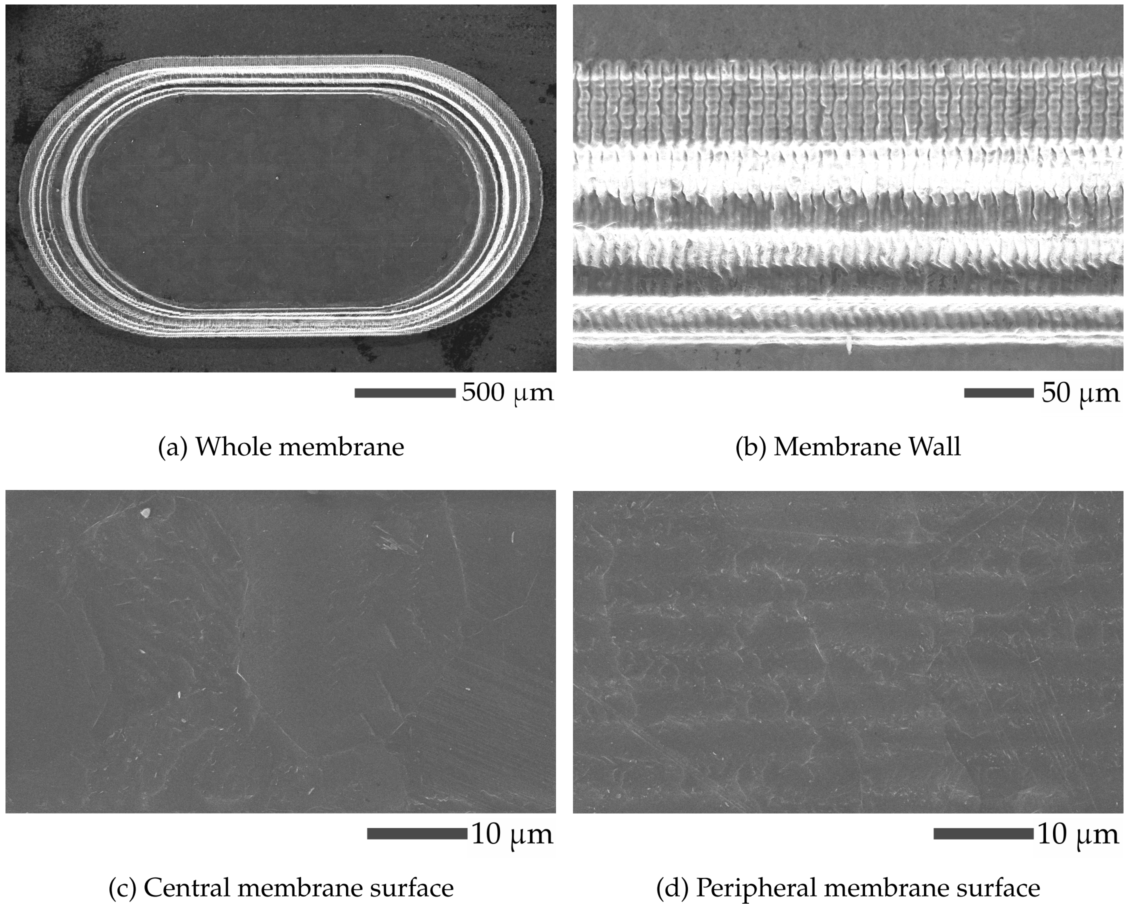

(a) Whole membrane

(b) Membrane Wall

(c) Central membrane surface

(d) Peripheral membrane surface

Figure 4.5: SEM micrographs of the laser-etched diamond membrane following H-plasma treatment. (a) Whole membrane, illustrating the stepped profile arising from sequential laser passes. (b) Wall region showing periodic microgrooves associated with the laser scan path. (c) Central membrane region, displaying a comparatively smooth surface indicative of effective post-processing. (d) Periphery of the membrane, where increased roughness and residual microgrooves from laser etching persist.

4.3.3.2 After BDD Growth

The characteristic microgrooves introduced by laser processing remained clearly visible after BDD growth as shown in Figure 4.6. The retained surface damage demonstrates that the newly grown diamond layer conformed to the underlying laser-induced morphology, which may affect the performance of the Schottky diode through increased roughness, structural non-uniformity, and a higher density of interfacial defects.

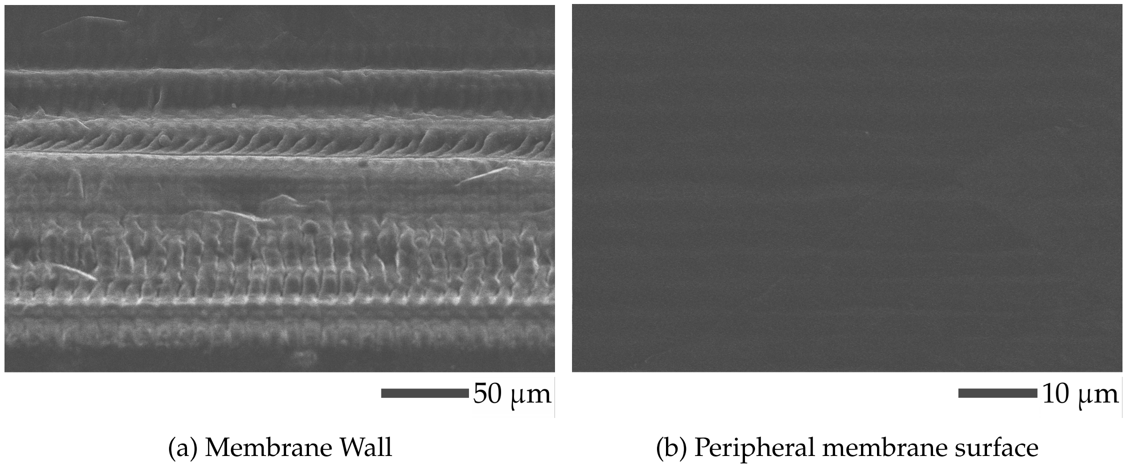

(a) Membrane Wall

(b) Peripheral membrane surface

Figure 4.6: SEM micrographs of the laser-etched diamond membrane following boron-doped diamond (BDD) growth. (a) Membrane wall, where periodic microgrooves and stepped laser profile remained evident. (b) Peripheral membrane surface, where roughness and laser-induced microgrooves were retained.

Chapter 5: Device Performance

5.1 Electron Gun

5.1.1 Overview

Simulated beta irradiation was performed using a Kimball Physics EGF-3104 electron gun. This flood beam system provides electrons with energies tunable from 1 to 20 keV, which were directed onto a substrate that was simultaneously electrically connected to a Keithley instrument via contact electrodes for in situ electrical measurements. This configuration enabled device characterisation under both biased and unbiased conditions, while the beam current and incident electron energy could be independently adjusted to suit the experimental requirements.

Electrons are produced via thermionic emission from a heated filament. The electron gun is connected to the EGPS-3104 unit containing all power supplies necessary to generate the voltages required. Of these, The focus element accelerates the electrons and causes the electron beam to diverge as it approaches the anode. The anode focuses the beam into multiple 'beamlets' through a mesh and affects the beam uniformity and divergence that reaches the substrate. The process is conducted under high vacuum conditions to minimise scattering of electrons by residual gas molecules, preserving beam energy and spatial resolution.

5.1.2 Data Acquisition

The sample was mounted in the electron gun holder and placed within the chamber, where it was left to pump down to vacuum overnight. A base pressure of 1×10^{-8} mbar was achieved prior to measurement.

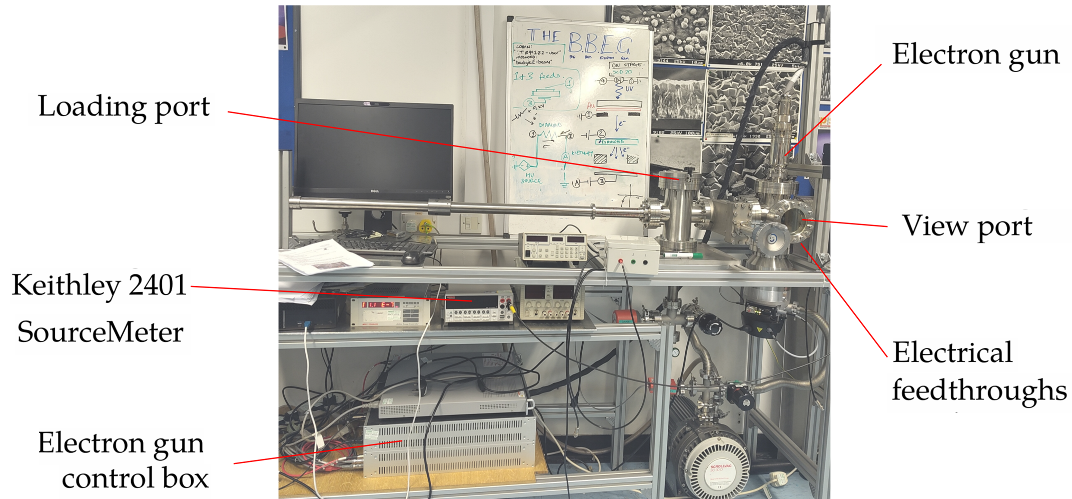

Figure 5.1: Electron-beam irradiation setup used for device testing, with key components indicated.

Once mounted inside the electron gun system shown in Figure 5.1, bias was applied to the device using a Keithley 1620 SourceMeter with a voltage range of ± 1000 V. Following equipment failure, this was replaced with a Keithley 2401 SourceMeter with a reduced range of ± 20 V. Data acquisition was automated using a custom Python script written by Dr Liam Cullingford. The applied voltage was swept from a defined start value to a final value, before being reversed back to the starting voltage. Forward bias is defined here as the polarity for which the Schottky metal is negative with respect to the back ohmic contact. At each voltage step, multiple current readings were recorded and averaged after a fixed settling time, summarised in Table 5.1. The voltage step size and number of readings per step were kept constant throughout all measurements. Dark current measurements were acquired prior to electron irradiation. Under irradiation, 5.7 keV electrons were first tested to represent the mean beta energy of tritium and therefore provide the principal assessment of low-energy sensitivity. This was followed by measurements from 1 to 20 keV in 1 keV intervals.

Table 5.1: Operating parameters of Electron Gun operation

Keithley	Value	Electron gun	Value
Voltage Range / V	±20	**1st Anode / V**	500
Voltage step / V	2	**Focus / V**	500
No. Readings per V	5	**Emission / mA**	0.8
Seconds to settle / s	1	**Max current / mI**	1.7

5.2 Initial Performance

5.2.1 5.7 keV

The initial electrical response of the device was evaluated by comparing the dark current to measurements obtained under 5.7 keV electron irradiation, as shown in Figure 5.2. It is clear that the leakage current and spectral noise is low enough to show impact of low energy tritium betas on the device. Under irradiation, the I-V response under forward bias showed a moderately sharp increase in current following a threshold voltage of 0 V. Under reverse bias, the magnitude of the current also increases under irradiation, demonstrating that charge carriers generated within the depletion region are effectively swept by the electric field. It is clear that the incident electrons generated a sufficient number of EHPs within the diamond to induce a measurable signal, confirming the functionality of the device as a beta detector. Notably, at approximately 1 V the current becomes negative, corresponding to a transient region where $IV < 0$. However, this effect is brief and is attributed to the release of stored charge, rather than steady-state power generation.

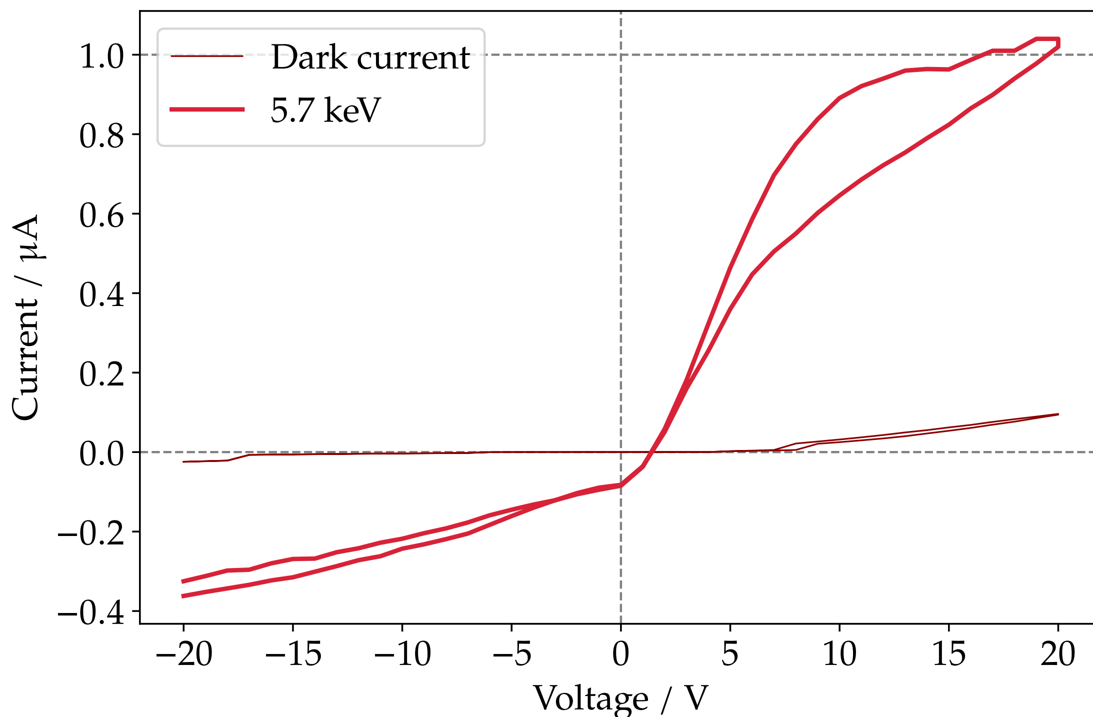

Figure 5.2: Current–voltage characteristics under dark conditions and under 5.7 keV electron irradiation. An increase in current is observed under irradiation in both forward and reverse bias, indicating successful generation and collection of charge carriers within the device.

5.2.1.1 Rectification Ratio

The rectification behaviour of the device was quantified at ±20 V, as shown in Table 5.2. A maximum forward current of 1.04 μA and reverse current of 0.325 μ yields a rectification ratio of 3.2. Compared with that recorded in literature,

it is a low value, as rectification ratios of 10^9 have been reported for single crystal Schottky diodes at 2 V [81], and 1000 for polycrystalline Schottky diodes [82] for dark current measurements. Whilst single crystal is expected to outperform polycrystalline due to its reduced defects, the orders of magnitude between this device and polycrystalline devices in literature is stark. Whereas a polished substrate was used in this work, Ref. [82] employed an unpolished substrate, avoiding the nanocrystalline damage expected to arise from polishing. As a result, the diodes in Ref. [82] likely exhibited larger surface crystallites and resulting Schotty junction with fewer graphitic surface defects, resulting in stronger rectification behaviour. Accordingly, forming the Schottky contact on the as-grown surface rather than the polished side may help narrow the gap between the rectification ratio obtained in this work and those reported in the literature.

Table 5.2: Rectification behaviour of the device at ±20 V

	I(+20 V) / µA	I(–20 V) / µA	Rectification Ratio
Initial test	1.04	0.325	3.2

5.2.1.2 Hysteresis

An obvious hysteresis was observed, with a lower absolute current on the reverse sweep than the forward sweep. Hysteresis have been reported for SiC devices [83–86] and has been attributed arise from electron trapping in interface states at the metal-semiconductor junction. During the forward sweep, electrons are stored in traps, however during the reverse sweep, not all traps have emitted their charges because the capture time is longer than the emission time [87]. In this work, the hysteresis is attributed to the graphitic impurities in polycrystalline diamond, which introduces defect states into the band gap of diamond and thus trapping the charge carriers and inducing the hysteresis observed. It has been reported that the magnitude of the hysteresis effect is shown to decrease with repeated I–V sweeping measurements [88], a phenomenon attributed to electron tunneling through the metal–semiconductor interface. Upon saturation of the interface traps, this "priming" effect reduces further trap filling and is therefore responsible for the reduced hysteresis.

5.3 Device Failure

Sequential I-V sweeping to examine the priming effect on hysteresis could not be performed due to the loss of diode characteristics between runs. The diode was removed from the E-beam chamber, and re-mounted 3 weeks later, where the dark current fluctuated around the pA range for the applied voltage with no forward voltage drop (Figure 5.3). This could be evidence of degradation during the previous run, where the SBH has been modulated due to build up of a space charge region of interface traps. However, visible scratching of the aluminium contact was observed, attributed to damage caused by the electron beam electrodes. This mechanical damage may have disrupted the uniformity of the interface, disrupting the electric field across the device. To investigate this,

the aluminium Schottky contact was removed using 5 ml nitrate etchant for 10 mins and subsequently re-deposited under the same fabrication conditions.

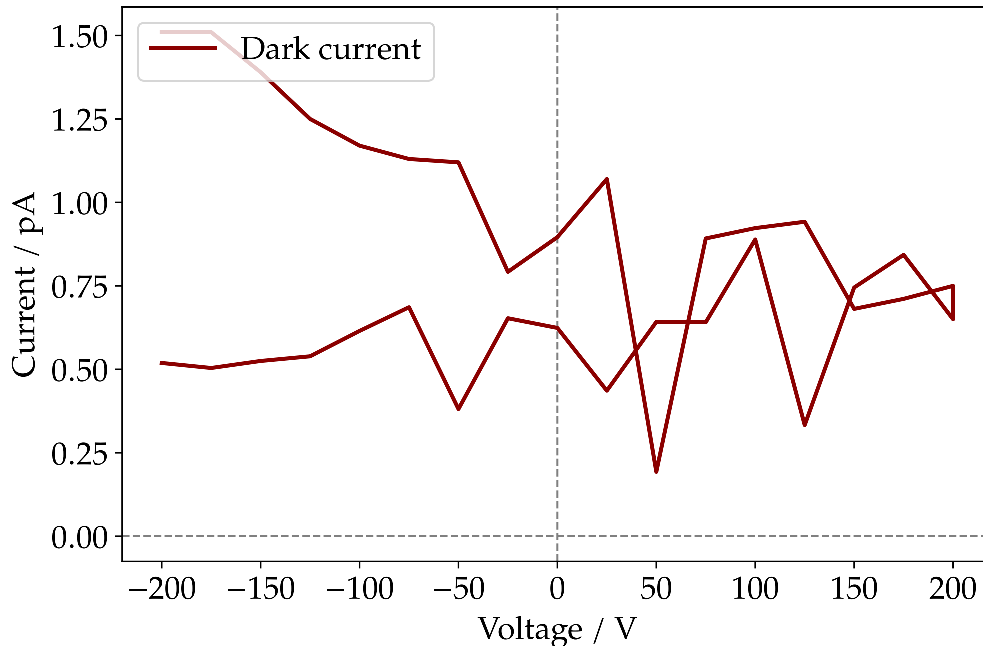

Figure 5.3: Dark current–voltage (I–V) characteristics of the device following degradation. The absence of rectification and the presence of low, unstable currents indicate failure of the Schottky junction.

5.4 Device Recovery

Following contact removal and re-deposition, the diode regained rectifying behaviour. The restoration of diode-like behaviour demonstrates that the observed failure originated from degradation of the Schottky contact rather than the diamond substrate. The restored device was subsequently used for energy-dependent measurements.

5.4.1 5.7 keV

Figure 5.4 compares the electrical response of the device before and after re-metallisation of the aluminium Schottky contact. The forward voltage drop remained the same at 0 V, however the gradient is significantly less steep and difference in current magnitude is observed between the two measurements, with the re-metallised device exhibiting 0.58 μA maximum current at 20 V compared with 1.04 μA previously. The differing I-V curves may be due to differing the current transport characteristics introduced by the different spatial inhomogeneity of the barrier height across the Schottky contact area of the two depositions. These results indicate that the electrical performance of polycrystalline diamond Schottky diodes is highly sensitive to contact quality, and that their reliable use will depend on reproducible contact fabrication.

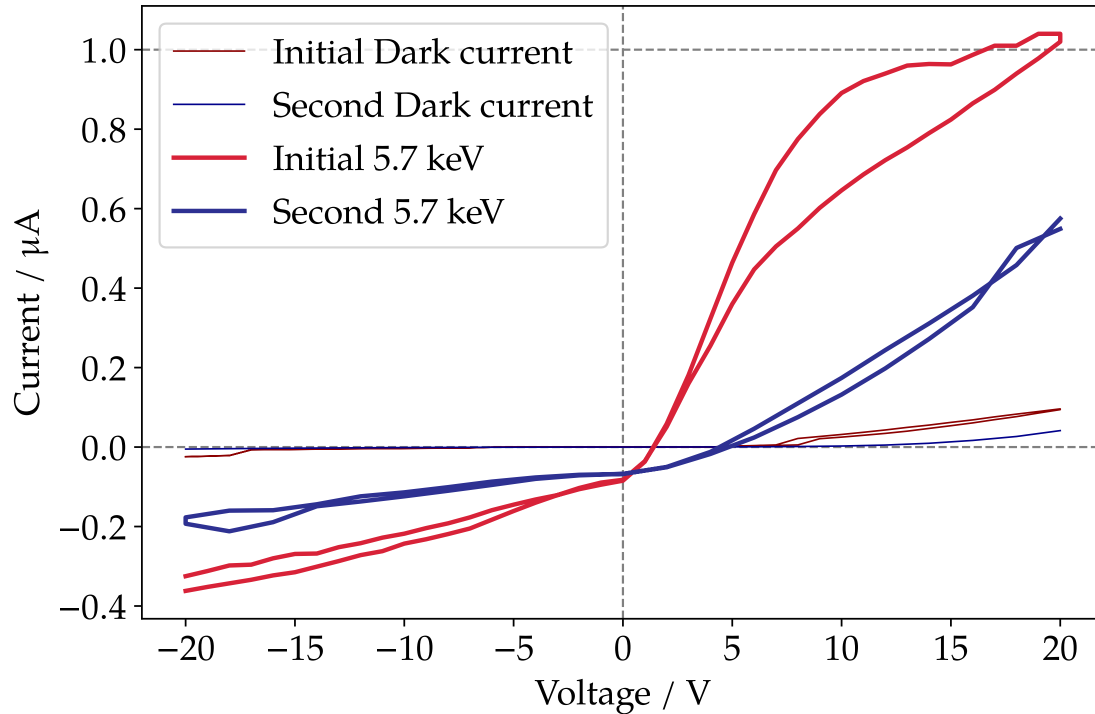

Figure 5.4: Current–voltage characteristics of the device before and after re-metallisation of the aluminium Schottky contact, under dark conditions and 5.7 keV irradiation. The restored rectifying behaviour confirms recovery of the Schottky junction following contact re-deposition.

5.4.1.1 Hysteresis

Notably, the reduced hysteresis after re-deposition suggests that the dominant contribution does not arise from grain-related trapping within the bulk diamond, but rather from traps associated with the surface or metal–semiconductor interface. The lower hysteresis implies a reduced trap density and therefore a more uniform Schottky barrier following contact replacement. As an acid clean was performed prior to oxygen termination and metal deposition to remove the previous metal contact, it is plausible that this step removed residual surface contamination not eliminated by oxygen termination, thus resulting in a more uniform Schottky contact.

5.4.1.2 Rectification Ratio

The rectification behaviour of the device before and after re-metallisation is summarised in Table 5.3. Although the absolute current decreased following contact re-deposition, the rectification ratio remained largely unchanged, from 3.20 to 3.25. This suggests that re-metallisation altered the overall conductance of the contact, but preserved the asymmetry between forward and reverse transport.

Table 5.3: Rectification behaviour at ±20 V of diode before and after re-deposition

	I(+20 V) / µA	I(–20 V) / µA	Rectification Ratio
Initial test	1.04	0.325	3.20
Second test	0.58	0.177	3.25

5.4.2 1–20 keV

The current–voltage characteristics across multiple beam energies are shown in Figure 5.5, and display a clear dependence of device response on incident electron energy with continued minimal hysteresis observed. As the energy increases from 1 to 20 keV, the measured current increases progressively, particularly under forward bias, indicating that higher-energy electrons give rise to greater charge generation within the diamond and hence a larger collected signal. The trend is not strictly linear, however, as the spacing between neighbouring curves varies across the energy range. In particular, the current at energies between 1 – 6 keV does not rise in order of increasing beam energy. This may be attributed to non-ideal transport environment in which grain boundaries, interface states, and local variations in electric field may all influence the fraction of generated charge contributing to the measured current, thus making the measurements unstable. By contrast, the more monotonic rise at higher energies indicates increasingly stable diode operation. In terms of application, an associated output current with a particular energy is crucial for energy resolution, and thus the non linearity between 1–6 keV indicates unstable diode operation.

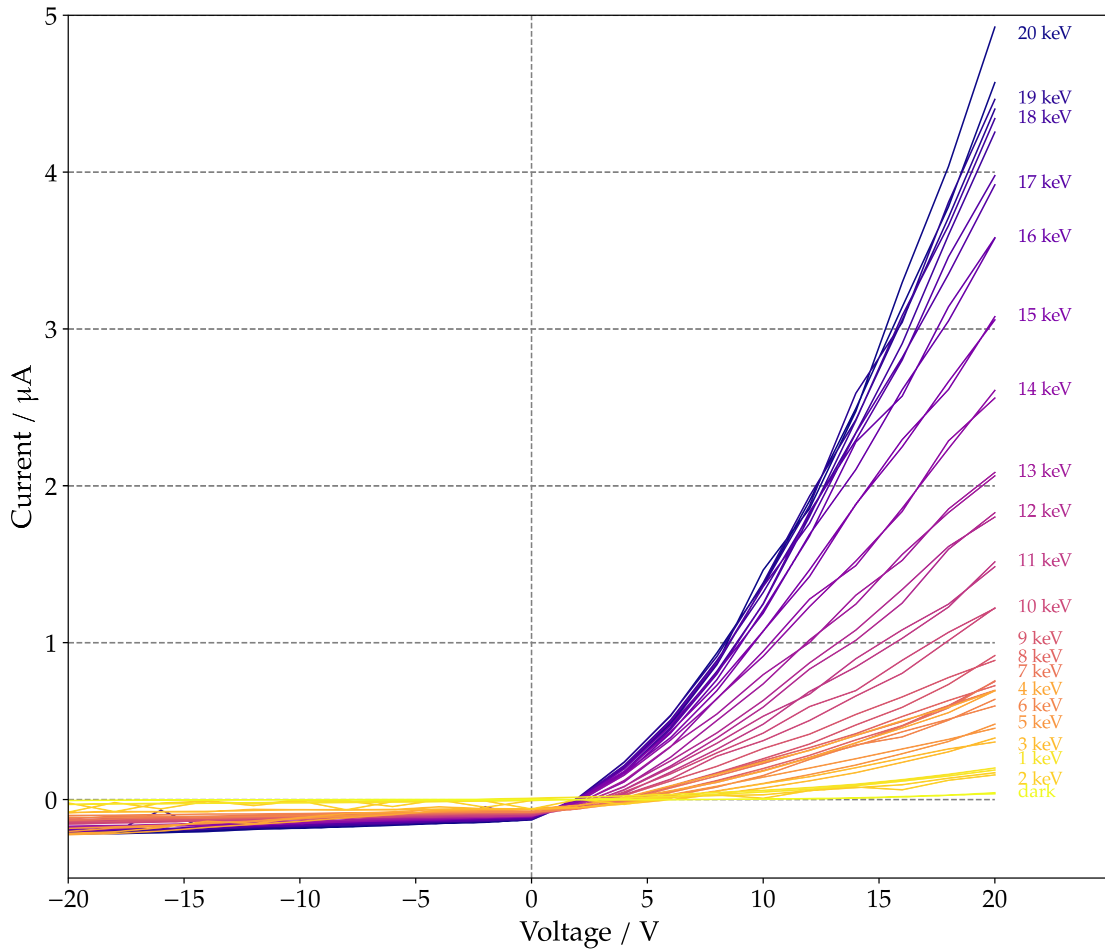

Figure 5.5: Current–voltage characteristics under dark conditions and under electron irradiation of energies 1–20 keV. An increase in current is observed under irradiation in both forward and reverse bias, indicating successful generation and collection of charge carriers within the device.

5.4.2.1 Rectification Ratio

The rectification ratio at each beam energy is shown in Figure 5.6 with exact values stated in the Appendix. An overall increase is observed across with increasing energy, rising from 2.1 at 2 keV to 22.6 at 20 keV. This indicates that increasing energy enhances not only the absolute current, but also the asymmetry between forward and reverse transport. The fluctuations in rectification ratio for energies between 1–6 keV are consistent with a non-linear increase in current, indicating that the device is operating near the limit of reliable discrimination. By contrast, incident energies above demonstrate a monotonic rise in rectification ratio, indicating that stable diode operation increases with incident energy above a discrimination limit of 6 keV.

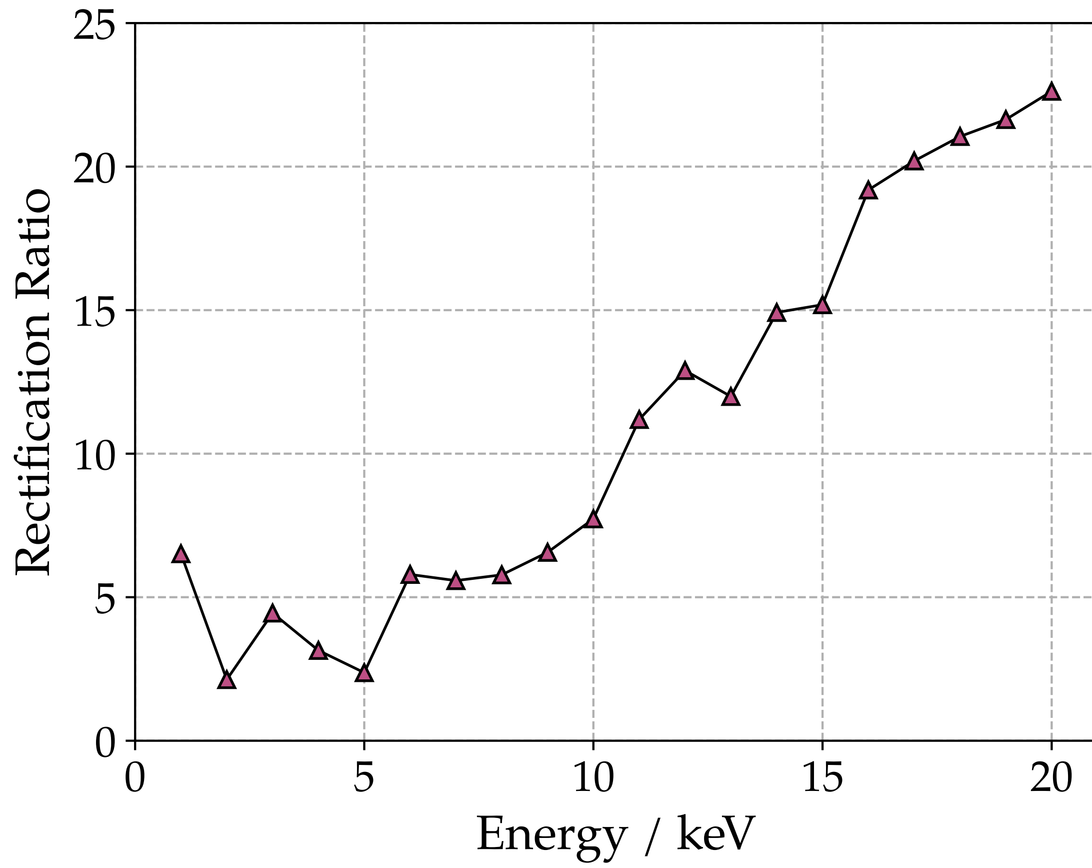

Figure 5.6: Rectification ratio measured at ±20 V from current–voltage characteristics recorded under incident electron beam energies of 1–20 keV.

Chapter 6: Conclusions & Future Work

6.1 Conclusions

A polycrystalline diamond Schottky diode was fabricated in this work with a membrane thickness of 33 μm and a 22.5 nm aluminium Schottky contact. Raman spectroscopy of the device revealed high polycrystalline quality with a prominent diamond peak at 1332 cm^{-1} with a FWHM of 7.9 cm^{-1}. The absence of boron-related features following BDD growth was unexpected, however a minor increase in FWHM to 8.1 cm^{-1} suggests a degree of structural disorder, which has been associated with boron incorporation elsewhere [71]. SEM imaging of the membrane surface revealed discernible polycrystalline grain structures in the central region and mild microgrooves in the periphery, indicating that low-power laser treatment followed by H-plasma CVD was least effective around the periphery, an effect attributed to limited access due to the membrane walls. The stepped profile of the walls demonstrated strong microgrooves that were remained following BDD growth, which may hinder EHP transport during device operation due to increased surface roughness and higher density of defects. Overall, this work has established a strong foundation for the laser micromachining of diamond membranes and demonstrated that laser micromachining is a viable fabrication route with clear potential for automation once the key processing parameters are optimised.

The device performance was evaluated *via* simulated beta irradiation using a EGF-3104 electron gun system across forward and reverse sweeps of applied bias between -20 and 20V. Initial testing at 5.7 keV revealed a measurable signal with a threshold voltage of 0 V, demonstrating the success of the diode in responding to incoming low energy beta radiation. A maximum forward current of 1.04 μA and reverse current of 0.325 μm at ±20 V yielded a rectification ratio of 3.2, which is several orders of magnitude lower than values reported for polycrystalline devices in the literature [82]. The low rectification ratio limits detector sensitivity and reduces the effectiveness of the device in practical sensing applications, and thus the device design may require optimisation. The device showed hysteresis which was attributed to the graphitic impurities in polycrystalline diamond, which introduces defect states into the band gap of diamond and thus trapping the charge carriers and inducing the hysteresis observed.

The device failed to operate following initial testing, an effect attributed to scratching due to the electron beam electrodes. For a detector eventually envisioned for long term deployment, this degradation cannot be written off as negligible and contact between the e-beam electrodes and metal contact something. Following contact removal and re-deposition, the diode regained rectifying behaviour, displaying the same turn on voltage of 0 V but reaching a reduced maximum amplitude of 0.58 μA. Despite this, the rectification ratio remained the same at 3.2, suggesting that re-metallisation altered the overall conductance of the contact but preserved the asymmetry between forward and reverse trans-

port. Notably, the hysteresis reduced, thus indicating that the original hysteresis observed was due to grain impurities on the surface as oppose to the bulk diamond. This highlights that incorporation of acid cleaning prior to metal deposition may enhance the Schottky barrier by eliminating impurities on the surface of the device.

Current–voltage characteristics across multiple beam energies highlight a clear dependence of device response on incident electron energy. Maximum current increased stepwise between 7–20 keV. However, at energies between 1–6 keV the maximum amplitude did not increase linearly with beam energy, an effect observed in the rectification ratio trends, where fluctuations in value between the energies of 1–6 keV suggested that the device was operating near the limit of reliable discrimination. No hysteresis was observed in the varying energy ranges, indicating that the Schottky barrier remained intact during measurement.

Overall, the device demonstrated real time monitoring, with spectral noise is low enough to show impact of low energy tritium betas on the device. This was a goal not accomplished by other devices in literature, and is very good. This study has demonstrated through good results that polycrystalline has potential as a cheaper alternative to single crystal for electronic devices. However, careful fabrication and design is required, as the incorporation of more traps through design (such as the stepwise membrane) introduces more defects into an already defected material, to which the EHP transport properties is very sensitive to, so significantly deteriorate performance.

6.2 Future work

The most significant direction for future work would be to evaluate the device under exposure to real beta-emitting radioisotopes. In the present work, operation in current mode measured only the total output current and therefore did not capture the pulse-based response that would arise from individual beta interactions. Pulse-mode measurements would allow individual events to be resolved and counted, providing more detailed detector information such as charge collection time. Since the duration of the pulse is determined by the time required for charge carriers to reach the electrodes, this would give insight into carrier drift and transport within the device [89]. In addition, integrating the output current pulse would allow the released charge, and hence the deposited energy, to be determined. This would provide data more directly relevant to practical beta detection applications.

Future work should focus on refining the device architecture to improve carrier transport. Three improvements are suggested here. Future designs should replace a stepwise membrane geometry with a smoother crater-like profile, which would reduce surface roughness and may improve EHP transport through the device, and may be achieved through use of a single laser template with a preprogrammed curved edge profile. A second would be to fabricate devices on the non-polished substrate face, where the larger crystal domains may provide less interrupted transport pathways, and has been noted to be effective approach in

other work [82]. In addition, the boron concentration in the present device was not determined in this work. Secondary ion mass spectrometry (SIMS) could be used to quantify the boron profile in this device and assess whether the doping level in the p-type layer was sufficient to produce a low-resistance ohmic contact. If the boron concentration is found to be below the metallic threshold of 10^{20} cm $^{-3}$ [90, 91], increasing the boron content during fabrication may improve contact conductivity, reduce series resistance, and enhance charge collection in future devices. Collectively, these modifications may improve rectification behaviour and bring device performance closer to that reported in the literature [82].

Whilst CASINO simulations accounted for the full energy range of low energy betas considered in this study, it was not possible to test energies above 20 keV as the GF-3104 electron gun was not configured for this purpose. Adapting the instrument to extend the experimental irradiation range to higher electron energies would allow a more complete validation of the simulated energy deposition behaviour across the full spectrum relevant to the isotopes considered.

A further area for investigation is the time dependence of device performance after irradiation. Repeated I–V measurements at defined intervals after the radiation source is removed would help determine whether the device returns reproducibly to its original electrical state, or whether residual charge trapping influences subsequent measurements. In addition, longer-term monitoring over extended periods would establish whether the signal output remains stable with time or exhibits drift. This would be important for assessing device reliability and repeatability in practical sensing applications.

The effect of temperature on detector performance should also be investigated. Since carrier transport depends on temperature through changes in mobility, trapping, and recombination behaviour, the electrical response of the device may vary under different operating conditions. Measuring the signal amplitude as a function of temperature would therefore provide useful calibration data and help establish whether temperature-dependent corrections are required when relating detector output to deposited beta energy.

Finally, since the CASINO simulations indicate that a thin Schottky metal layer is required, the diamond surface must be sufficiently smooth to enable uniform metal deposition. Future work could therefore include quantitative surface roughness analysis, for example using surface-sensitive techniques at the NanoESCA. The influence of surface roughness on metal continuity, interface uniformity, and the resulting built-in electric field could then be investigated. This would help establish whether local topographical variation contributes to non-uniform contact formation and induces variability in device performance.

Bibliography

[1] F. Zhao, Y. He, B. Huang, T. Zhang and H. Zhu, *Materials*, 2024, **17**, 3437.

[2] S. Xi, C. Zhou, Y. Zhang, H. Li, Z. Wang, Z. Liu, X. Yi and J. Li, *Radiation Effects and Defects in Solids*, 2023, **178**, 938–955.

[3] H. Quiroga-Barriga, F. Nápoles-Rivera, C. Ramírez-Márquez and J. M. Ponce-Ortega, *Processes*, 2025, **13**, 2654.

[4] Z. P. Putra, H. A. Pratama, R. Sumarbagiono, G. Nurliati, M. Romli, S. Bakhri, B. Setiawan, N. S. Pamungkas and M. Yusuf, *Nuclear Engineering and Technology*, 2025, 103828.

[5] M. F. Ngulimi, S. Kim, K. Asghar, B. K. Seo and C. Roh, *Advanced Energy and Sustainability Research*, 2025, **6**, 2400243.

[6] W. S. Li, R. Z. Li, Y. Zhang, X. W. Zhang, R. J. Sun, X. Wang, L. J. Zhang and S. D. Zhang, Fifth International Conference on Mechanical Engineering and Materials (ICMEM 2024), 2025, pp. 601–614.

[7] A. R. Whittemore and E. M. Zannoni, *Sensors*, 2025, **25**, 1776.

[8] N. Mukhamedov, K. Toleubekov, G. Vityuk, M. Bekmuldin and S. Dolzhikov, *Energies*, 2025, **18**, 3486.

[9] K. Asghar, M. F. Ngulimi, S. Kim, B. K. Seo and C. Roh, *Chemical Engineering Journal Advances*, 2024, **20**, 100668.

[10] S. Mukhopadhyay, R. Maurer and P. Guss, Hard X-Ray, Gamma-Ray, and Neutron Detector Physics XXII, 2020, p. 114940B.

[11] M. de Lafontaine, C. Succar, R. F. H. Hunter, G. P. Forcade, J. P. D. Cook, J. Patel, B. Ellis, H. Fritzsche, J. J. Krich and K. Hinzer, *Cell Reports Physical Science*, 2025, **6**, 102789.

[12] S. Xi, C. Zhou, Y. Zhang *et al.*, *Applied Physics A*, 2024, **130**, 753.

[13] E. B. Agyekum, *Journal of Energy Storage*, 2025, **122**, 116701.

[14] Z. Ding, T.-X. Jiang, R.-R. Zheng, N. Wang, L.-F. Zhang, S.-C. Liu, X. Li and H.-S. San, *Nuclear Science and Techniques*, 2022, **33**, 144.

[15] R. Zheng, Z. Ding, W. Wang, N. Wang, Z. Wang, T. Jiang, X. Li, S. Liu, L. Zhang and H. San, *Applied Surface Science*, 2023, **611**, 155757.

[16] S. Liu, P. I. Theoharis, R. Raad, F. Tubbal, A. Theoharis, S. Iranmanesh, S. Abulgasem, M. U. A. Khan and L. Matekovits, *Electronics*, 2022, **11**, 2021.

[17] K. McMullan, J. Paxman, R. M. Howie and S. Loffler, *Acta Astronautica*, 2026, **238**, 550–568.

[18] T. R. Alam, M. T. Tchouaso and M. A. Prelas, in *Photovoltaics for Space*, ed. S. G. Bailey, A. F. Hepp, D. C. Ferguson, R. P. Raffaelle and S. M. Durbin, Elsevier, 2023, pp. 293–345.

[19] C. Thomas, S. Portnoff and M. G. Spencer, *Applied Physics Letters*, 2016, **108**, 013505.

[20] S. I. Maximenko, J. E. Moore, C. A. Affouda and P. P. Jenkins, *Scientific Reports*, 2019, **9**, 10892.

[21] D. L. Wagner, D. R. Novog and R. R. LaPierre, *Journal of Applied Physics*, 2020, **127**, 244303.

[22] M. Wu, S. Wang, Y. Ou and W. Wang, *Applied Radiation and Isotopes*, 2018, **142**, 22–27.

[23] S. Wei, Y. Wei, J. Wang, S. Yan, W. Wang, Z. Ma and C. Li, *Nuclear Science and Engineering*, 2024, **199**, 465–475.

[24] Z.-J. Cheng, H.-S. San, X.-Y. Chen, B. Liu and Z.-H. Feng, *Chinese Physics Letters*, 2011, **28**, 078401.

[25] G. Wang, R. Hu, H. Wei, H. Zhang, Y. Yang, X. Xiong, G. Liu and S. Luo, *Applied Radiation and Isotopes*, 2010, **68**, 2214–2217.

[26] S. Butera, G. Lioliou and A. M. Barnett, *Applied Radiation and Isotopes*, 2017, **125**, 42–47.

[27] S. Butera, M. D. C. Whitaker, A. B. Krysa and A. M. Barnett, *Semiconductor Science and Technology*, 2018, **33**, 105003.

[28] F. Bouzid, S. Dehimi, M. Hadjab, M. A. Saeed and F. Pezzimenti, *Physica B: Condensed Matter*, 2021, **607**, 412850.

[29] F. Bouzid, M. A. Saeed, R. Carotenuto and F. Pezzimenti, *Applied Physics A*, 2022, **128**, 234.

[30] M. Böhles, S. Böser, M. Eisenhuth, C. Girard-Carillo, K. M. H. Curiel, B. Keßler, K. Mossel, V. Palušová, A. Weber, M. Wurm and S. Schoppmann, *European Physical Journal C*, 2025, **85**, 755.

[31] J. W. Poston, in *Encyclopedia of Physical Science and Technology*, ed. R. A. Meyers, Academic Press, New York, 3rd edn., 2003, pp. 603–650.

[32] J. Tölgyessy and M. Harangozó, in *Encyclopedia of Analytical Science*, ed. P. Worsfold, A. Townshend and C. Poole, Elsevier, Oxford, 2005, pp. 16–24.

[33] International Atomic Energy Agency, *IAEA Nuclear Data Services*, n.d., https://www-nds.iaea.org/, accessed April 2026.

[34] K. Asghar, M. F. Ngulimi, S. Kim, B. K. Seo, G. H. V. Bertrand and C. Roh, *Progress in Materials Science*, 2026, **158**, 101616.

[35] M. F. L'Annunziata, in *Radioactivity*, ed. M. F. L'Annunziata, Elsevier Science B.V., Amsterdam, 2007, pp. 119–140.

[36] G. B. Saha, in *Physics and Radiobiology of Nuclear Medicine*, Springer, 2006, pp. 71–80.

[37] G. F. Knoll, *Radiation Detection and Measurement*, John Wiley & Sons, 1979.

[38] Revvity, Inc., *Tri-Carb 4910TR Liquid Scintillation Counter: Specifications*, https://www.revvity.com, 2023, accessed March 2026.

[39] Hidex Oy, *Hidex 300 SL Automatic TDCR Liquid Scintillation Counter: Specifications*, https://www.hidex.com, 2020, accessed March 2026.

[40] O. Piraner and R. L. Jones, *Journal of Radioanalytical and Nuclear Chemistry*, 2021, **330**, 381–384.

[41] Berthold Technologies GmbH & Co. KG, *LB 110 Tritium Monitor: Product Information*, https://www.berthold.com, 2019, Id. No. 80872PR2, Rev04, accessed March 2026.

[42] R. A. Myers, R. Farrell, F. Robertson, D. Dogruel and R. S. Willms, *Proceedings of SPIE*, 2008, **7080**, 70800C.

[43] D. Siegmann, F. Edzards, C. Bruch, M. Biassoni, M. Carminati, M. Descher, C. Fiorini, C. Forstner, A. Gavin and M. Gugiatti, *Journal of Physics G: Nuclear and Particle Physics*, 2024, **51**, 085202.

[44] S. Mertens, T. Brunst, M. Korzeczek, M. Lebert, D. Siegmann, A. Alborini, K. Altenmüller, M. Biassoni, L. Bombelli and M. Carminati, *Journal of Physics G: Nuclear and Particle Physics*, 2021, **48**, 015008.

[45] M. Moszyński, A. Syntfeld-Każuch, Ł. Swiderski, M. Grodzicka, J. Iwanowska, P. Sibczyński and T. Szczéśniak, *Nuclear Instruments and Methods in Physics Research Section A*, 2016, **805**, 25–35.

[46] G. Bertuccio and F. Mele, *IEEE Transactions on Nuclear Science*, 2023, **70**, 2310–2321.

[47] T. Baba, N. F. Hasbullah, N. Saidin *et al.*, *Transactions on Electrical and Electronic Materials*, 2025, **26**, 779–800.

[48] Mirion Technologies, *DT D - XPR80 On-Line Tritium Detector*, https://www.mirion.com/fr/products/technologies/radiation-monitoring-systems/detectors-and-custom-channels/dt-d-xpr80-on-line-tritium-detector, accessed March 2026.

[49] Mirion Technologies, *HT Ionix Tritium Bubbler*, https://www.mirion.com/fr/products/technologies/radiation-monitoring-systems/tritium-measurement/tritium-samplers/ht-ionix-tritium-bubblers, accessed March 2026.

[50] R. Marie-Luce, P. Mai, F. Lerouge *et al.*, *Nature Photonics*, 2024, **18**, 1037–1043.

[51] A. Kumar, M. K. Paswan, P. Panda and A. Agarwal, *Proceedings of the National Academy of Sciences, India Section A: Physical Sciences*, 2025.

[52] A. Traoré, *PhD thesis*, Université de Grenoble, 2014.

[53] M. Schwander and K. Partes, *Diamond and Related Materials*, 2011, **20**, 1287–1301.

[54] Y. Liu, J. He, N. Zhang, W. Zhang, Y. Zhou and K. Huang, *Journal of Materials Science*, 2021, **56**, 12559–12583.

[55] M. Suzuki, T. Sakai, T. Makino, H. Kato, D. Takeuchi, M. Ogura, H. Okushi and S. Yamasaki, *Physica Status Solidi A*, 2013, **210**, 2035–2039.

[56] E. Abubakr, S. Ohmagari, A. Zkria, H. Ikenoue, J. Pernot and T. Yoshitake, *Materials Research Letters*, 2022, **10**, 666–674.

[57] B. Liu, B. Dai, K. Liu, L. Yang, J. Zhao, G. Shu, Z. Lv, G. Gao, K. Yao, M. Bi, J. Xue, W. Wang, V. Ralchenko, J. Han and J. Zhu, *Diamond and Related Materials*, 2018, **87**, 35–42.

[58] B. Liu, K. Liu, V. Ralchenko, D. Dzmitrovich, L. Yang, Y. Yang, X. Zhang, Z. Su, J. Zhao, G. Shu, G. Gao, K. Yao, M. Bi, S. Zhang, J. Xue, W. Wang, J. Han, J. Zhu and B. Dai, *International Journal of Energy Research*, 2019, **43**, 6038–6044.

[59] V. S. Bormashov, S. Y. Troschiev, A. P. Volkov, S. A. Tarelkin, E. Korostylev, A. Golovanov, M. Kuznetsov, D. Teteruk, N. Kornilov, S. Terentiev, S. Buga and V. Blank, *physica status solidi (a)*, 2015, **212**, 2539–2547.

[60] V. S. Bormashov, S. Y. Troschiev, S. A. Tarelkin, A. P. Volkov, D. V. Teteruk, A. V. Golovanov, M. S. Kuznetsov, N. V. Kornilov, S. A. Terentiev and V. D. Blank, *Diamond and Related Materials*, 2018, **84**, 41–47.

[61] D. Drouin, A. R. Couture, D. Joly, X. Tastet, V. Aimez and R. Gauvin, *Scanning*, 2007, **29**, 92–101.

[62] P. W. May, *Philosophical Transactions of the Royal Society A: Mathematical, Physical and Engineering Sciences*, 2000, **358**, 473–495.

[63] Evident Corporation, *LEXT OLS5100 3D Measuring Laser Microscope*, 2024, https://www.olympus-ims.com/.

[64] S. Prawer and R. J. Nemanich, *Philosophical Transactions of the Royal Society A: Mathematical, Physical and Engineering Sciences*, 2004, **362**, 2537–2565.

[65] A. Dychalska, P. Popielarski, W. Franków, K. Fabisiak, K. Paprocki and M. Szybowicz, *Materials Science-Poland*, 2015, **33**, year.

[66] C. V. Hernández, *Introduction to Raman Spectroscopy and Its Applications*, Springer, Cham, 2025.

[67] C. A. Taylor, M. F. Wayne and W. K. S. Chiu, *Thin Solid Films*, 2003, **429**, 190–200.

[68] J. Shin, C. S. Lee, K. Lee and K. Y. Eun, *Applied Physics Letters*, 2001, **78**, 631–633.

[69] A. C. Ferrari and J. Robertson, *Physical Review B*, 2000, **61**, 14095–14107.

[70] D. R. McKenzie, R. N. Tarrant, M. M. M. Bilek, T. Ha, J. Zou, W. E. McBride, D. J. H. Cockayne, N. Fujisawa, M. V. Swain, N. L. James, J. C. Woodard and D. G. McCulloch, *Diamond and Related Materials*, 2003, **12**, 178–184.

[71] T. R. Anthony, *Diamond and Related Materials*, 1995, **4**, 1346–1352.

[72] F. Pruvost and A. Deneuville, *Diamond and Related Materials*, 2001, **10**, 531–535.

[73] J. Xia, L. Gu, S. Ye, S. Zhang, Z. Ye, M. Ye, C. Zhao, S. Gu and Y. Hang, *Diamond and Related Materials*, 2026, **162**, 113327.

[74] V. Mortet, Z. V. Živcová, A. Taylor, O. Frank, P. Hubík, D. Trémouilles, F. Jomard, J. Barjon and L. Kavan, *Carbon*, 2017, **115**, 279–284.

[75] J. Filik, *Spectroscopy Europe*, 2005, **17**, year.

[76] V. N. Apakina, A. L. Karuzskii, M. S. Kogan, A. V. Kvit, N. N. Melnik, Y. A. Mityagin, V. N. Murzin, A. A. Orlikovsky, A. V. Perestoronin, S. D. Tkachenko and N. A. Volchkov, *Diamond and Related Materials*, 1997, **6**, 564–568.

[77] D. S. Knight and W. B. White, *Journal of Materials Research*, 1989, **4**, 385–393.

[78] R. N. Tarrant, O. Warschkow and D. R. McKenzie, *Vibrational Spectroscopy*, 2006, **41**, 232–239.

[79] R. Haubner and M. Rudigier, *Physics Procedia*, 2013, **46**, 71–78.

[80] J. Filik, J. N. Harvey, N. L. Allan, P. W. May, J. E. P. Dahl, S. Liu and R. M. K. Carlson, *Physical Review B*, 2006, **74**, 035423.

[81] V. Grushko, O. Beliuskina, A. Mamalis, V. Lysakovskiy, E. Mitskevich, A. Kiriev, E. Petrosyan, R. Chaplynskyi, O. Bezshyyko and O. Lysenko, *Applied Radiation and Isotopes*, 2020, **157**, 109017.

[82] D. Shinyavskiy, C. Wang, L. Suter, M. Muehle and J.-H. Seo, *Advanced Electronic Materials*, 2025, **11**, e00409.

[83] F. Devynck, A. Alkauskas, P. Broqvist and A. Pasquarello, *Physical Review B*, 2011, **84**, 235320.

[84] A. J. Lelis, D. Habersat, R. Green, A. Ogunniyi, M. Gurfinkel, J. Suehle and N. Goldsman, *IEEE Transactions on Electron Devices*, 2008, **55**, 1835–1840.

[85] G. Rescher, G. Pobegen, T. Aichinger and T. Grasser, 2016 IEEE International Electron Devices Meeting (IEDM), 2016, pp. 10.8.1–10.8.4.

[86] S. U. Omar, T. S. Sudarshan, T. A. Rana, H. Song and M. V. S. Chandrashekhar, *IEEE Transactions on Electron Devices*, 2015, **62**, 615–621.

[87] A. Vasilev *et al.*, 2020 IEEE International Integrated Reliability Workshop (IIRW), 2020, pp. 1–4.

[88] H. Yuan, Q.-W. Song, C. Han, X.-Y. Tang, X.-N. He, Y.-M. Zhang and Y.-M. Zhang, *Chinese Physics B*, 2019, **28**, 117303.

[89] M. Nakhostin, *Signal Processing for Radiation Detectors*, John Wiley & Sons, 2017.

[90] E. Kohn, W. Ebert, A. Aleksov, A. Denisenko, M. Adamschik and P. Schmid, Proceedings of the 23rd International Conference on Microelectronics, 2002, pp. 59–66.

[91] M. Sultana, S. Karmakar and A. Haque, *Materials Science in Semiconductor Processing*, 2025, **186**, 109024.

Chapter 7: Appendix

Table 7.1: Rectification ratio at ±20 V for energies 1–20 keV

Energy	RR	Energy	RR	Energy	RR	Energy	RR
1 keV	6.5	6 keV	5.7	11 keV	11.3	16 keV	19.8
2 keV	2.1	7 keV	6.0	12 keV	13.1	17 keV	20.2
3 keV	4.7	8 keV	5.9	13 keV	11.9	18 keV	20.2
4 keV	3.1	9 keV	6.5	14 keV	15.2	19 keV	21.5
5 keV	2.4	10 keV	7.9	15 keV	14.7	20 keV	22.6